Summer 2020

Computational Elucidation of the "Coloring Problem" in Rhenium Aluminum Silicon Compounds

Alec George Neeson
Missouri State University, Alec777@live.missouristate.edu

COMPUTATIONAL ELUCIDATION OF THE "COLORING PROBLEM" IN RHENIUM ALUMINUM SILICON COMPOUNDS

A Master's Thesis

Presented to

The Graduate College of

Missouri State University

In Partial Fulfillment

Of the Requirements for the Degree

Master of Science, Chemistry

By

Alec George Neeson

August 2020

COMPUTATIONAL ELUCIDATION OF THE "COLORING PROBLEM" IN RHENIUM ALUMINUM SILICON COMPOUNDS

Chemistry Department

Missouri State University, August 2020

Master of Science

Alec George Neeson

ABSTRACT

$Re_1Si_1Al_1$ and its related compounds are potential thermoelectric materials. Previously, it was reported to adopt a $MoSi_2$-type structure with Si and Al atoms statistically sharing the same crystallographic sites. This recent study indicates otherwise – Si and Al are segregated and occupy different sites when mixed with a 1:1:1 stoichiometry. To confirm and rationalize the segregation between Si and Al, this research studied this compound with first-principle calculations. Several model structures have been constructed for $Re_1Si_1Al_1$ including a number of different super-cell models. Energy analysis confirmed that the model with Si/Al segregation has the lowest energy. The chemical bonding in $Re_1Si_1Al_1$ was investigated by computing Crystal Overlap Hamilton Populations (COHPs) and comparing the band structures of the models. It was found that low energy models typically possess a bandgap. The valence electron density maps were calculated to investigate the origin of the bandgaps. Bonding appears to play the largest factor in the 1:1 structures. These computations should provide more insight into the nature of $Re_1Si_1Al_1$ and its related compounds.

KEYWORDS: solid-state chemistry, computational chemistry, thermoelectric materials, crystallography, physical chemistry, materials science

COMPUTATIONAL ELUCIDATION OF AN ANOMALOUS RHENIUM SILICON ALUMINUM CRYSTAL STRUCTURE'S FORMATION

By

Alec George Neeson

A Master's Thesis
Submitted to the Graduate College
Of Missouri State University
In Partial Fulfillment of the Requirements
For the Degree of Master of Science, Chemistry

August 2020

Approved:

Fei Wang, Ph.D., Thesis Committee Chair

Besara Tiglet, Ph.D., Committee Member

Matthew Siebert, Ph.D., Committee Member

Kartik Ghosh, Ph.D. , Committee Member

Julie Masterson, Ph.D., Dean of the Graduate College

ACKNOWLEDGEMENTS

I would like to thank the support of my graduate studies to Dr. Fei Wang

TABLE OF CONTENTS

LIST OF TABLES

LIST OF FIGURES

CHAPTER 1 INTRODUCTION

Currently, a crisis exists in the modern world of sustainable energy. Effects of global energy expenditure include global warming, ozone depletion, as well as oil shortages.[1] Thermoelectric materials are thought to be promising in relief of the current energy crisis for several reasons. One reason is that implementation of thermoelectric devices allow for more energy efficiency.[2] For instance, typical diesel engines are only approximately 45 % efficient, leaving the bulk of energy loss as waste heat, part of which can be recycled with thermoelectric generators.[3] Also, thermoelectric devices have the potential to innovate refrigeration techniques by reducing the application of environmentally threatening chemicals, such as chlorofluorocarbon (CFC's) coolants which could cause the destruction of the ozone layer.[4] Thermoelectric implementations prove to be promising in a wide range of applications ranging from industrial power production industry to microelectronics.[5]

1.0 Thermoelectric Phenomena

Thermoelectric phenomena have been observed for almost two centuries. These effects were discovered by Thomas Seeback as well as Jean Peltier in the early 1800s. Experimentally, it was observed that in a closed loop circuit, a temperature difference in the material would deflect the needle of a compass. It was shown that this deflection of the magnetic field was due to an induced current in the wire. Later, this effect was shown to be reversible and an electrical current could cause a temperature gradient thus allowing for thermoelectric coolers. The Seeback coefficient is taken to be the ratio of a temperature difference in a material typically in Kelvin versus the electrical voltage.

Several materials, typically inorganic, have been shown to possess thermoelectric properties. Some of the first materials include compounds of bismuth, lead, zinc, antimony, tellurium, and several others. Research of thermoelectric materials has expanded upon these basic elements considerably to include materials ranging from inorganic compounds of BiTe to functionalized graphene as well as nanostructures such as quantum dots and carbon nanotubes.[6][7] Overall, the effectiveness of these materials are quantified by a figure of merit, namely ZT.[8] Where S is the Seeback coefficient, σ is the electrical conductivity, T is the temperature, and κ is the thermal conductivity. This figure of merit helps to quantify the efficiency of the thermoelectric material in question. Typically a material with ZT > 1 is possible to integrate into the economy.[9]

$$ZT = S^2\sigma\, T/\, \kappa$$

1.1 Motivation of $Re_1Si_1Al_1$ Materials

Rhenium silicide ($ReSi_{1.75}$) with aluminum doping has previously been shown to be a promising thermoelectric material.[10][11] It has been found that doping $ReSi_{1.75}$ with 2% Al obtains a ZT value of 0.95 at 1073 K. This aluminum doping has been shown to increase electrical conductivity (σ), reduce thermal conductivity (κ), as well as increase the Seeback coefficient (S), which all contribute to the increase of ZT. Further investigations into these materials could lead us to deeper understanding of these compounds and help to design and synthesize more efficient thermoelectric materials.

The crystal structure of $ReSi_{1.75}$ is a supercell variant of the $MoSi_2$-type structure (Figure 1.1). Compared to $MoSi_2$, $ReSi_{1.75}$ is missing some Si atoms. These Si atom missing, or Si vacancies, are ordered and give rise to a much larger unit cell. The Al-doped variants of $ReSi_{1.75}$

have similar Si vacancies but the amounts of the vacancies are different and they are also ordered in different manners. After doping, the crystal structures become incommensurate.

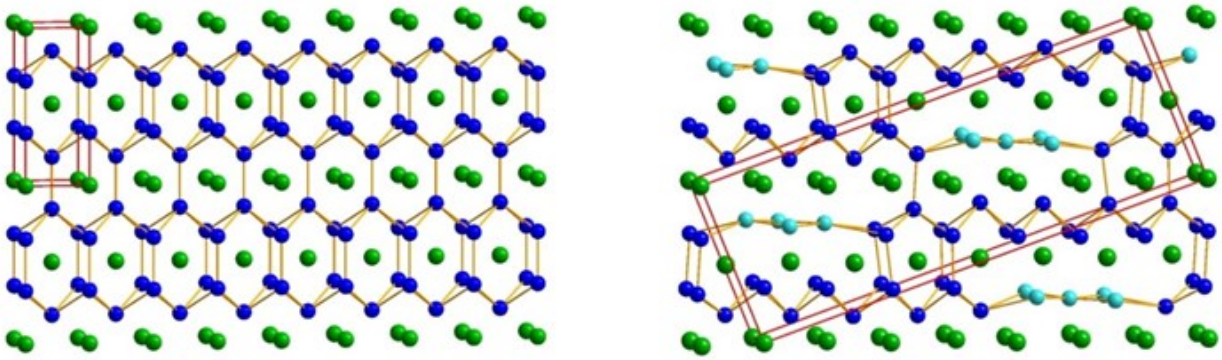

Figure 1.1 The crystal structures of $MoSi_2$ (left) and $ReSi_{1.75}$ (right). Atoms: green – Mo and Re; dark and light blue – Si. The light blue atoms highlight the difference between the two structures. The red boxes are the unit cells.

These complicated crystal structures caused by Si vacancies are expected to give rise to low lattice thermal conductivity (κ), which is one of the most probable reasons why these materials are promising in thermoelectric applications. The Si vacancies arise due to the (18 – n) electron rule, which is commonly observed for compounds between transition metals and main group elements.[12],[13] In these compounds, the rule states that every transition metal atom, such as Re and Mo, should have (18 – n) valence electrons. 18 comes from the complete filling of the s, p, and d subshells and n is the number of homoatomic bonding between the transition metal atoms. For $MoSi_2$ and $ReSi_{1.75}$, n = 4 because each Mo/Re has 4 neighboring Mo/Re (left, right, front, and back) in their crystal structures. So the number of electrons per transition metal atom is 18 – 4 = 14. In $MoSi_2$, Mo has 6 valence electrons and there are 2 portions of Si so, totally, $6 + 2 \times 4 = 14$. In $ReSi_{1.75}$, Re has 7 valence electrons and not 2 but only 1.75 portions of Si are needed to achieve 14 electrons, $7 + 1.75 \times 4 = 14$. This is why $ReSi_{1.75}$ has Si vacancies compared to

$MoSi_2$. When doping with Al, because Al has 1 less electron per atom than Si, the amount of vacancies can be reduced. For instance, when we have $Re_1Si_1Al_1$, there are exactly 7 + 3 + 4 = 14 valence electrons and it is 1 portion of Re and 2 portions of Al/Si, no vacancy at all.
We decided to study $Re_1Si_1Al_1$ because it is expected to have no vacancies and assume the same simple structure as $MoSi_2$. Thus, by comparing $Re_1Si_1Al_1$ with $ReSi_{1.75}$ and its complicated Al-doped variants, we will be able to confirm and evaluate the role played by the complicated crystal structures and Si vacancies in the latter.

$Re_1Si_1Al_1$ was successfully prepared with arc melting. Its unit cell is shown in Figure 1.2. Indeed, its structure resembles $MoSi_2$. However, there is a subtle difference. $MoSi_2$ has a body-centered tetragonal (I4/mmm) unit cell while $Re_1Si_1Al_1$s unit cell is primitive (P4/nmm). The seemingly body-centered Re atom is not precisely at the center. It is farther away from the top Re and closer to the bottom Re (Figure 1.2, left). This is in contrast with a previous report about $Re_1Si_{0.8}Al_{1.2}$ (Figure 1.2, right), which does adopt the body-centered tetragonal unit cell, just like $MoSi_2$.

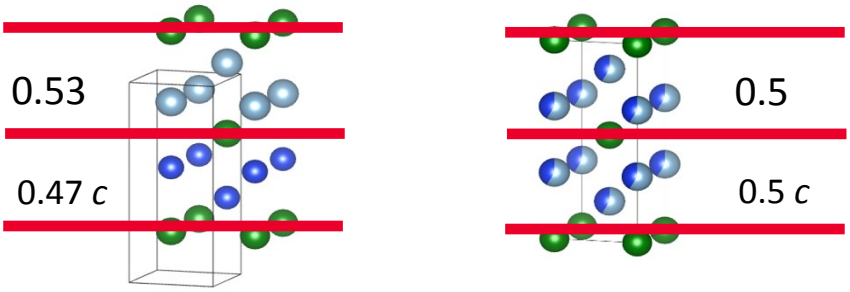

Figure 1.2 $Re_1Si_1Al_1$ (left) and $Re_1Si_{0.8}Al_{1.2}$ (right) experimentally determined structures. Green – Re; dark blue – Si; light blue – Al. The red lines show that the unit cell is not body centered for $Re_1Si_1Al_1$ but is body-centered for $Re_1Si_{0.8}Al_{1.2}$.

To confirm that $Re_1Si_1Al_1$ and $Re_1Si_{0.8}Al_{1.2}$ are indeed different even though their compositions are so close, both compounds were made again and compared with single crystal

diffraction. Figure 1.3 shows the 1*kl* planes of their diffraction patterns, which clearly shows that, compared to $Re_1Si_1Al_1$, the pattern of $Re_1Si_{0.8}Al_{1.2}$ misses half of the reflections. These systematic absences prove that, indeed, $Re_1Si_1Al_1$ is primitive and $Re_1Si_{0.8}Al_{1.2}$ is body-centered (see Figure 1.4 for neutron diffraction).

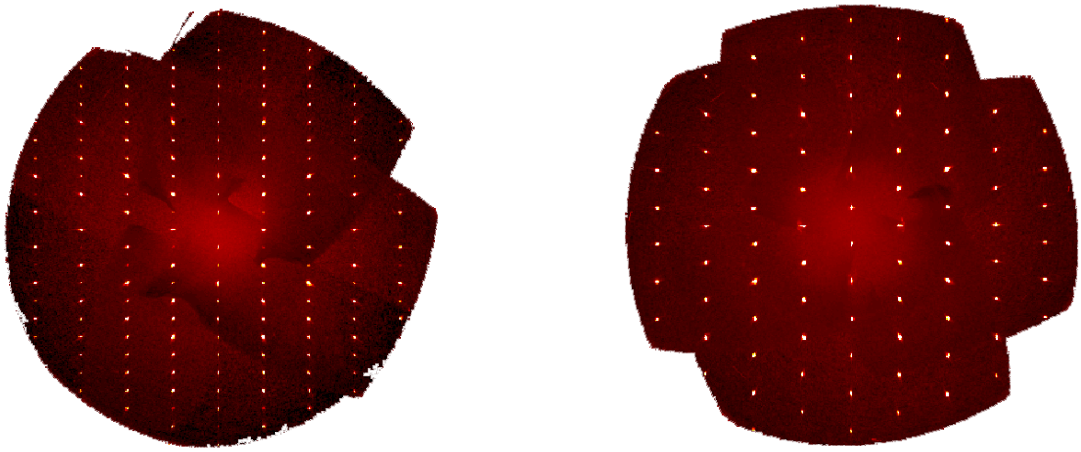

Figure 1.3 The 1*kl* planes of the single crystal diffraction patterns of $Re_1Si_1Al_1$ (left) and $Re_1Si_{0.8}Al_{1.2}$ (right).

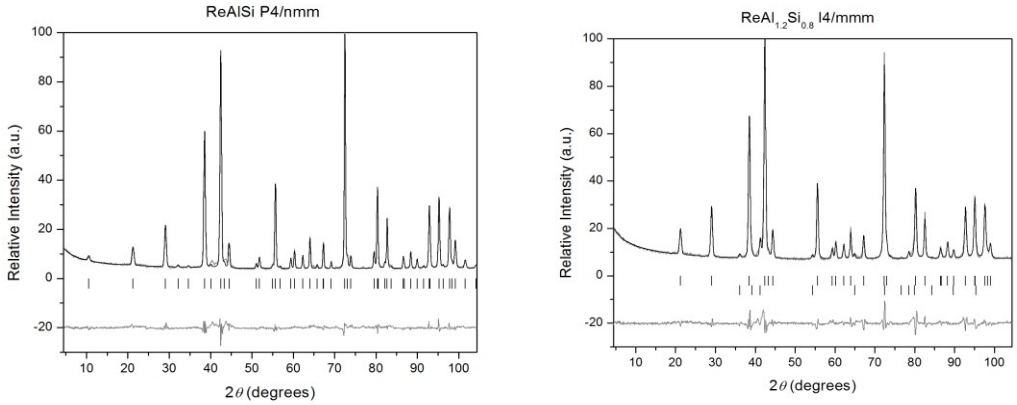

Figure 1.4. Neutron diffraction patterns of $Re_1Si_1Al_1$ (left) vs. $Re_1Si_{0.8}Al_{1.2}$ (right).

The reason why $Re_1Si_{0.8}Al_{1.2}$ are so different, as elucidated by the Rietveld refinements of their neutron diffraction patterns, is because Al and Si are segregated (ordered) in $Re_1Si_1Al_1$. As shown in Figure 1.2, the top half of the unit cell has only Al and the bottom half has only Si. Because Si atoms are smaller than Al, the central Re atom is closer to the bottom than to the top. By comparison, in $Re_1Si_{0.8}Al_{1.2}$, the Al and Si are disordered and randomly distributed on the same crystallographic sites (Figure 1.2).

This difference between $Re_1Si_1Al_1$ and $Re_1Si_{0.8}Al_{1.2}$ is intriguing. Therefore, before we study the physical properties of $Re_1Si_1Al_1$, we would like to figure out why its Al and Si atoms are segregated but not randomly mixed as in $Re_1Si_{0.8}Al_{1.2}$.

The question at hand is to understand and explain these observed different crystal structures between $Re_1Si_1Al_1$ and $Re_1Si_{0.8}Al_{1.2}$. In order to rationalize it, computational methods were implemented. These methods are quantum mechanical in origin but can be interpreted via moderately simple chemical arguments with computational information. These computational algorithms will briefly be discussed in this first chapter. In the second chapter the methodology of this investigation will be considered. And lastly the computational results will be presented and discussed in the third and fourth chapter.

1.2 Beginnings of Quantum Understanding

Historically, the origin of chemistry was largely experimental and empirical. Theoretical understanding of chemistry largely did not begin until the development of quantum physics in the early 1900s. Max Planck's theory regarding fundamental units of electromagnetic energy elucidated an extremely small (in magnitude) but very important constant known as Planck's constant (h).

$$h = 6.626 \times 10^{-34} \text{ Joules•seconds}$$

This constant defined a sort of discrete unit of energy known as a quantum. Einstein experimented with light and published in 1905 evidence that light could be treated as a particle of energy by the equation:

$$E = h\nu$$

Many scientists then realized that the physical understanding of extremely small matter and energy could not be comprehended from physical modeling of macroscopic phenomena. This different physical modeling is described by quantum physics. Furthermore, DeBroglie had the epiphany that not only could light experimentally behave as waves and particles, but also that particles could behave like waves leading him to the relationship of a particle's momentum and its corresponding wavelength λ.

$$\lambda = \frac{h}{mv}$$

Several important discoveries (too many to discuss here) were made along the way in the discovery of this exotic physics. In 1925 Werner Heisenberg and Erwin Schrödinger independently discovered matrix and wave mechanics of quantum physics respectively. Chemists generally are introduced to Schrödinger's wave mechanics through a deceptively simple equation.

$$H\psi = E\psi$$

This eigenvalue equation is typically for solving stationary states (where energy has no temporal dependence) of electrons and quasi-particles. H is the Hamiltonian operator, generally represented as:

$$H = T + V$$

Where T is the kinetic energy operator and V is the potential energy operator of the Hamiltonian respectively. $\Psi(x,t)$ is the total wave function representing a sort of probability amplitude whereas $\psi(x)$ typically represents only the spatial part of the wavefunction for the steady state solution. Also, in Schrödinger's equation, E simply represents the scalar value of energy. Ideally the Schrödinger equation solved analytically or numerically can give one ample information about a collection of quantum particles such as electrons, nuclei, and photons. However, once there are more than three particles, this equation cannot be solved analytically. Many numerical methods as well as simplifying assumptions are applied to this equation in order to obtain reasonable results of such systems.

One such simplifying assumption is the Born-Oppenheimer approximation. This approximation suggests that due to the nuclei being much more massive than the electrons, the nuclear coordinates can simply be removed as they are relatively constant in comparison with electrons. After this approximation, the Hamiltonian reduces to its electronic analog:

$$H = -\sum_{i=1}^{N}\frac{1}{2}\nabla_i^2 - \sum_{i=1}^{N}\sum_{A=1}^{M}\frac{Z_A}{r_{iA}} + \sum_{i=1}^{N}\sum_{j>i}^{N}\frac{1}{r_{ij}}$$

This general Hamiltonian, shown with Hartree units, contains N number of electrons, M number of nuclei, and varying distances of N and M particles specified by r_{iA} and r_{ij}. The first summation represents the kinetic energy.[14][15] The second two summations represent the potential energy of the nuclei and electron interactions. Whereas the third two summations represent the electron-electron interactions which generally is much more difficult to deal with. *Ab initio* methods solve equation 1 with the electronic Hamiltonian and no further simplifications. It is not difficult to imagine how challenging this task becomes in a crystal where there are moles of atoms interacting with one another.

Having mentioned the Hamiltonian operator, it should be noted that there are actually a wide variety of operators in the description of quantum physics. The wave function can be operated on by any of these operators and produce an expectation value in the form $< \Psi|O| \Psi>$ where O is a generic operator, and Ψ is the wavefunction. If the wavefunction is not normalized then this operation must be divided by $< \Psi| \Psi>$ to normalize the wavefunction and find the corresponding expectation value.

Before any further discussion, one very useful computational technique should be mentioned. This is known as the variational principle. Because the Schrödinger equation is a many body problem, generally it is not possible to solve analytically. The variational principle states that a trial wavefunction's energy $<\Psi^*_{trial}|E|\Psi_{trial}>$ will always be greater than or equal to the real wavefunction's energy $<\Psi^*_{real}|E|\Psi_{real}>$. Although other methods exist for algorithmically approximating Schrödinger's equation (perturbation theory for example), the variational method computationally speaking, is convenient. Realistically, one could use any function desired to approximate the wavefunction of a certain chemical system. However, typically the initial function implemented is a reasonable guess in terms of what is already known about the types of atoms in the chemical system under investigation.

Although not previously mentioned, the methods introduced thus far for solving the Schrödinger equation are based on a wavefunction method. The general idea behind wavefunction methods are to solve for a set of two electron wavefunctions approximately and use them to calculate any observable properties desired based on corresponding operators. There are a wide variety of wave function methods not mentioned here including the Hartree-Fock method. Typically, the total wavefunction that one is approximating depends upon 3N variables where N is the number of electrons in the procedure. It is easy to imagine how daunting this task

might be even for small molecules such as acetone (there are 32 total electrons making for as many as 100 Hamiltonian terms).

1.3 Rise of Density Functional Theory

In an attempt to simplify this procedure, Pierre Hohenburg, Lu Sham, and Walter Kohn, published papers in 1964 and 1965 to prove such a method exists by way of two theorems.[16][17] Simply put, their first theorem stated that there exists a functional depending upon electronic density $\rho(\mathbf{r})$ that is equivalent to the ground state energy of Schrödinger's equation. In essence, this means that the ground state electronic density $\rho(\mathbf{r})$ can be used to determine all other properties of the system under investigation too. This includes the wave function. At first sight this seems to be promising because the electronic density is only dependent upon three variables where wave-functional methods depended upon 3N (or more with spin of electrons). However, there was no insight whatsoever on what this functional actually was, only that it depended upon the function of electronic density and that it exists.

The second theorem proved that the electronic density that minimizes this functional the most corresponds directly to the true electronic density of the whole system. Interestingly, these proofs show that one does not need to solve for each electron's wavefunction independently but solve for the total wavefunction all at once. This idea can be shown by the Kohn-Sham equation:

$$\left[\frac{h^2}{2m}\nabla^2 + V(\mathbf{r}) + V_H(\mathbf{r}) + V_{\mathrm{XC}}(\mathbf{r}) \right] \psi_i(\mathbf{r}) = \varepsilon_i \psi_i(\mathbf{r})$$

It can be seen that the organization of this equation is very similar to the Schrödinger Equation.[18] Note however that no summations exist in the Hamiltonian because one is not finding each electron's individual wavefunction anymore. $V(\mathbf{r})$ represents the relation of the

electron attraction to the nuclei. $V_H(\mathbf{r})$ represents the Hartree potential. This potential is defined by the electronic repulsion of the total density and a single electron. Because the density includes the single electron being considered, there is a correction in $V_{xc}(\mathbf{r})$ for this since it is not reasonable. $V_{xc}(\mathbf{r})$ also includes all exchange and correlation terms as well as any form of the energy not included already. Exchange and correlation of quantum mechanical systems typically are not exactly known.

1.4 Exchange and Correlation Functional Considerations

Because the form of $V_{xc}(\mathbf{r})$ is not known exactly to this day, approximations must be implemented. One of the first kinds of approximations considered was that of a uniform electron gas. For a uniform electron gas the density $n(\mathbf{r})$ is constant everywhere and known analytically. The approximation method known as local density approximation (LDA) defines at each sampling point that the $V_{xc}(\mathbf{r}) = V_{xc}$ of the homogenous electron gas. There are several other functionals to approximate the exchange-correlation energy in DFT calculations shown below. John Perdew compares an assortment of these functionals to Jacob's Ladder from the bible. Each rung represents a step closer to "Heaven" where the true exchange-correlation potential is obtained. One thing that can be seen from this is that each higher rung typically includes an additional dependence on electronic density. Note that there are many different functionals used for each type. For instance generalized gradient approximation (GGA) methods might be implemented with Perdew-Wang or Perdew-Burke-Ernzerhof functionals. One might think that going to a higher run of this version of Jacob's ladder (Figure 1.5.) correlates with higher accuracy. This is simply not always the case however. Whenever implementing functionals of the meta-GGA or hyper-GGA type there might not be a general representation for the system

under study. For instance, some higher functionals implement empirical fitting parameters that pertain to the system under study. These typically are very costly calculations that are only relevant to the particular system that the parameters have been optimized for.

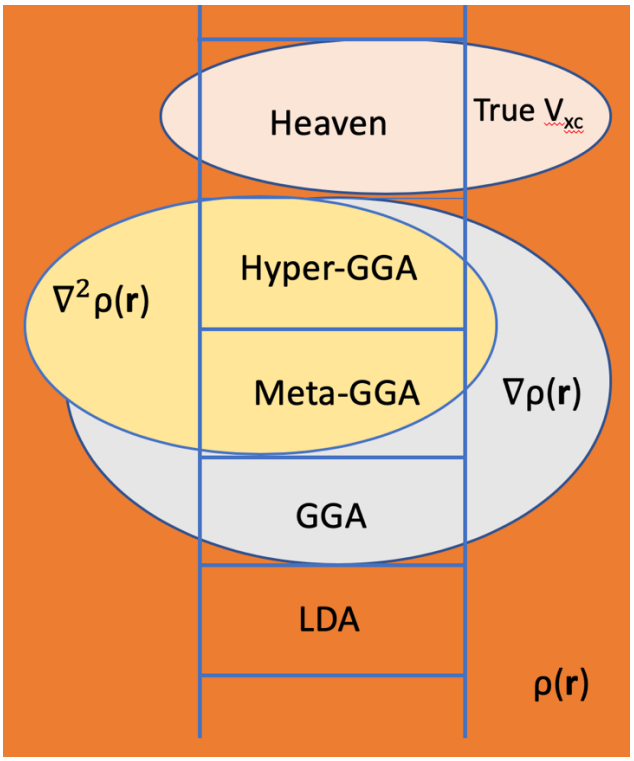

Figure 1.5 Jacob's Ladder for DFT exchange-correlation functionals

1.5 Kpoints

In computations presented in this paper, calculations are employed via k-space. This idea can be abstract to one not familiar with such concepts. Bloch's theorem states that the wavefunction of a repeating array of atoms (typically an electron in a crystal lattice) can be of the form:

$$\Psi_k(\mathbf{r}) = \Psi_k(\mathbf{r}+\mathbf{T}) = e^{i\mathbf{kr}}\,\Psi_k(\mathbf{r})$$

Where **T** is an arbitrary translation vector, **r** is position vector, and **k** is the reciprocal lattice vector.[19] It can be seen that wavefunction's of this form possess plane wave characteristics. Typically a DFT calculation involves solving integrals over this k-space. In 1976 , Monkhorst and Pack developed a solution/algorithm to solving these types of integrals.[20] One only has to specify the number of *kpoints* along each of the reciprocal lattice vectors in order to use this algorithm. Typically there are an optimal number of these points to implement. If too many are used than the computations take much longer than needed and do not improve results much. If too few *kpoints* are used then the results are not accurate. One must treat their system under study accordingly. Since k-space has an inverse dependence on real space then increasing the size of the unit cell for instance, should mean that fewer *kpoints* will be needed.

1.6 Energy Cutoffs in DFT

Recalling Bloch's Theorem, it is seen that periodic wavefunction's can be expressed with plane waves. Furthermore, this periodicity allows for the wavefunctions to be expanded into a form as:

$$\Phi_{\kappa} = \sum_{\boldsymbol{G}} c_{k+G}\, e^{i(\boldsymbol{k}+\boldsymbol{G})\boldsymbol{r}}$$

Where **G** is a reciprocal space vector. The summation goes over all possible **G** values which there are infinite many. Solutions of this equation with the Schrödinger equation yields a kinetic energy equivalent to:

$$E = \frac{h}{2m}^{2} |\boldsymbol{k}^2 + \boldsymbol{G}^2|$$

Reasonably, it is understood that lower energy values of kinetic energy are more reasonable and in this infinite sum, therefore a cutoff limit is defined $\mathbf{G}_{\text{cut}}$. This limits the number of values

summed in the plane wave summation. Energy cutoff values allow for the computation to not include an infinite sum which would clearly be incomputable. Typically, a limit is reached where increasing the $\mathbf{G}_{cut}$ has virtually no effect on the convergence of the computation.

1.7 Pseudopotentials

Approximately, core electrons do not have a significant effect on the interaction between two or more atoms. Because of this, an approximation known as a pseudopotential is implemented into standard calculations for ease of time. There are several different types of pseudopotentials including the Plane Augmented Wave Method (PAW) potentials used in this study.[21] Some of these potentials are calculated *ab initio* beforehand and assumed to be relatively constant while others are empirically fitted to several parameters.

1.8 Total Energy Calculations

The objective of DFT calculations is to solve for the ground state electronic density $\rho(\mathbf{r})$. This density can then determine all other desired properties of the system under study with the right quantum operators. Vaguely, a computation consists of defining an initial guess for $\rho(\mathbf{r})$. This estimate of electronic density is then used to define the effective potential of the system $V_{eff}(\mathbf{r})$ from the Kohn-Sham equation. After solving the defined Kohn-Sham equations, a new density is defined, and total energy related to this density. If the energy of the new and old density differs by less than a defined amount of tolerance, then $\rho(\mathbf{r})$ is considered to be solved for otherwise the cycle continues until subsequent energies are within tolerance of each other.

In order to introduce COHP (crystal orbital Hamilton population), firstly Mulliken's population should be considered first.[22][23][24] For two atomic orbitals φ, a molecular orbital can be expressed as

$$\Psi = c_i \varphi_i + c_j \varphi_j$$

That is a linear combination of atomic orbitals (LCAO). If one considers the electronic density (Ψ^2) then this produces

$$\Psi^2 = c^2_i \varphi^2_i + 2c_i c_j \varphi_i \varphi_j + c^2_j \varphi^2_j$$

where $c^2_i \varphi^2_i$ is the electronic density for atomic orbital i and $2c_i c_j \varphi_i \varphi_j$ represents the overlap electronic density of the orbitals. For a crystal if two specific atoms are specified, then their crystal orbitals can be used to compute their overlap populations. This is considered COOP (crystal orbital overlap population).

For COHP, the populations are no longer just overlap of wavefunctions but are weighted with the Hamiltonian operator. For the same wave function above, $\Psi = c_1\varphi_1 + c_2\varphi_1$, its energy E is calculated as:

$$E = <\Psi|H|\Psi> = <c_1\varphi_1 + c_2\varphi_2|H|c_1\varphi_1+c_2\varphi_2> = c^2_1E_1 + c^2_2E_2+2c_1c_2<\varphi_1|H|\varphi_2>$$

Where E_1 and E_2 are the energy (eigenvalues) of φ_1 and φ_2, and H is the Hamiltonian operator. The $2c_1c_2<\varphi_1|H|\varphi_2>$ term is a measure of the energy change caused by the interaction between φ_1 and φ_2. If this term is negative, their interaction lowers the energy (bonding). If it is positive, the interaction raises the energy (antibonding). For a crystal, these terms are COHPs, which provides a quantitative evaluation of bonding energies. Typically one has to specify the COHP for pairs of atoms in the crystal. The wave functions with delocalized plane wave basis sets are projected onto localized ones such as Slater type orbitals and from there the COHP is computed.

For ease of explanation (and visualization in Figure 1.6), one might consider an infinite one-dimensional chain of hydrogen atoms.[25] The density of states (DOS) represents a weighting of the electronic states within the band structure. It can be seen that the most available electronic states are at the flattest parts of the bands. COOP is simply the DOS weighted with the amount of overlap of the crystal orbitals. This is positive for bonding type interaction, and negative for antibonding, as well as zero for nonbonding. Not only can the weighting of the DOS be done with overlap populations, but also of energy populations. COHP (crystal orbital Hamilton population) is simply weighting the electronic energy states of the DOS with their corresponding band structure energy producing a COHP curve. If one integrates COOP or COHP curves to the fermi level, then one obtains the ICOOP (integrated crystal orbital overlap population), or ICOHP (integrated crystal orbital Hamilton population), which are simply single numbers representing the crystal's overall electronic overlap or energy contribution.

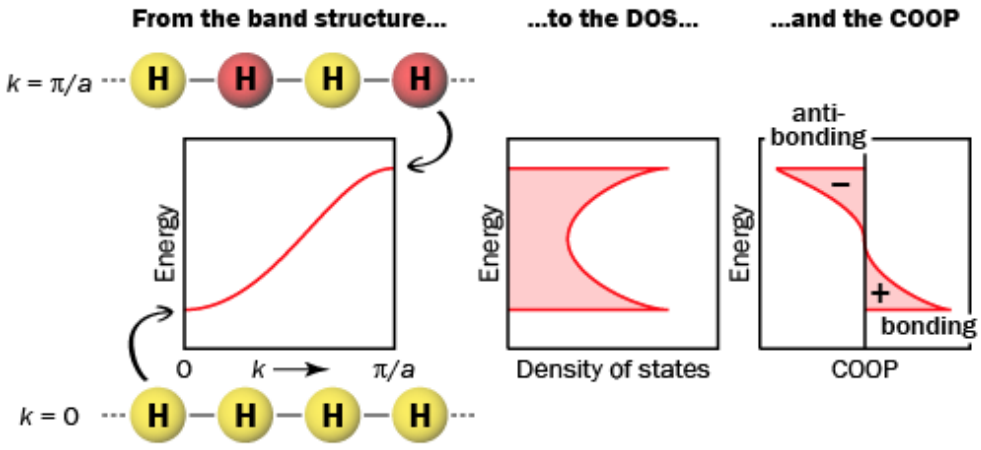

Figure 1.6 Bandstructure of one-dimensional infinite chain of hydrogens (left), Density of States (middle), COOP curve (right)

1.9 Concluding remarks

Throughout this introduction several concepts have been introduced briefly. The take away message from all this is that $Re_1Si_1Al_1$ compounds unexpectedly form different crystal structures based on slight changes to stoichiometric ratios. These crystal structures were investigated computationally to determine why this is the case. The general methods of these computations have been briefly mentioned. Chapter 2 will discuss specific parameters of the computation and the general idea of this study's approach. Chapter 3 and 4 will discuss results and rationalize the observation that these $ReSi_xAl_y$ compounds form distinct structures.

CHAPTER 2 METHODLOGY

2.0 The "Coloring Problem"

"Coloring problem" is a concept borrowed by solid state chemistry from graph theory.[26] It addresses how atoms of different elements are arranged in a given crystal structure and, more importantly, why they are arranged in certain ways. The question being studied in this thesis comprise a typical "coloring problem" – why are Al and Si atoms segregated in $Re_1Si_1Al_1$ but randomly distributed in $ReSi_{0.8}Al_{1.2}$.

The study a "coloring problem" usually relies on are computational techniques by comparing model crystal structures with different arrangements of atoms. In this experiment, several artificial models were made *via* a software called Visualization for Electronics and Structural Analysis *(*VESTA).[27] These models had the same composition of $Re_1Si_1Al_1$. The Rhenium sites were held constant whereas the Aluminum and Silicon sites were varied. These sites were varied in such a way to allow for more or less segregation. For instance, two model structures are shown in Figure 2.1. If we examine the Al and Si atoms as layers separated by Re atoms, the model on the left has Al and Si in each layer but the model on the right has alternating Si and Al layers. So the one on the right has Al and Si more segregated and the one on the left has them more mixed.

By comparing model structures with different degree of Al/Si segregation/mixing, we will be able to see why Al and Si segregation occurs in $Re_1Si_1Al_1$. In order to explore more possibilities of segregations and mixing, several super cells were also made. These include 112 (1 × 1 × 2), 211 (2 × 1 × 1), 212 (2 × 1 × 2), and 221 (2 × 2 × 1) where each integer represents a scaling factor of the basic crystal unit cell dimensions: *a*, *b*, and *c*.

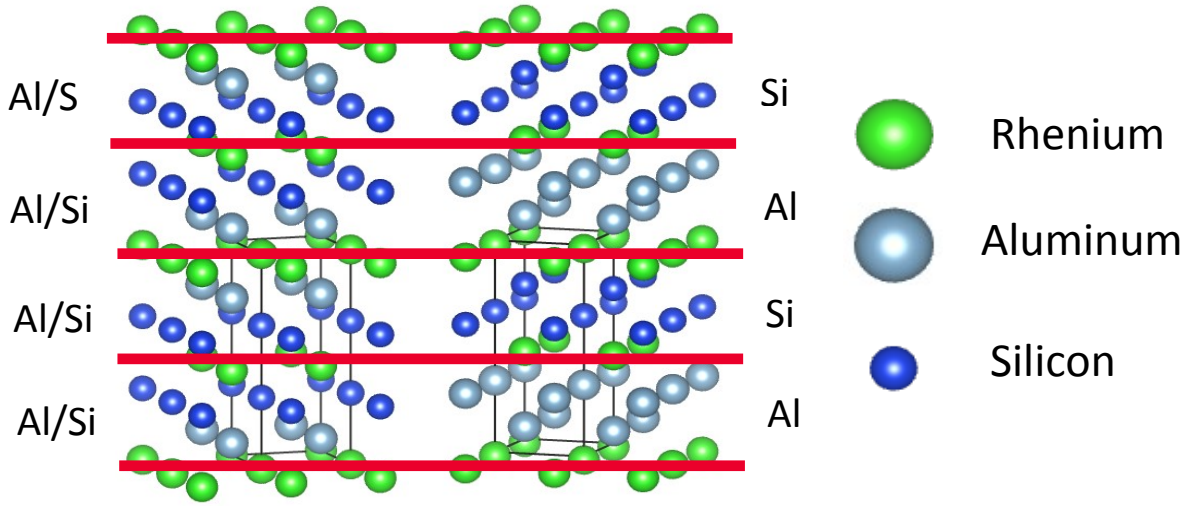

Figure 2.1 $Re_1Si_1Al_1$ models 111_1 (left) & 111_2 (right)

2.1 Parameters

Vienna Ab Initio Software Package (VASP) was used to compute energies of these artificial structures.[28][29][30] There were several parameters used in VASP that need to briefly be mentioned. Psuedopotentials were implemented for each Rhenium, Silicon, and Aluminum with the projector augmented-wave method (PAW). Electronic exchange-correlation is treated with the Perdew-Burke-Ernzerhof (PBE) generalized gradient approximation (GGA) method.[31] The energy cutoff for the plane waves (energy cutoff keeps the basis set finite), which was taken to be 306.7 electron Volts. In the KPOINTS file (used for sampling the reciprocal space of the crystal structure), the automatic monkhorst package mentioned in the introduction was used. Also, considering each super crystal cell, different amounts of kpoints were used in order to adjust for the different sizes of the unit cell as shown below in Table 2.1. K-space has an inverse dependence in comparison to real-space so for a larger super cell, fewer k-points were needed. All geometry optimizations were repeated until less than 4 iterations were needed using the

conjugate gradient method. During geometry optimizations the unit cell volume was fixed to the experimental values obtained. These experimental values are shown for different model sets in Table 2.2.

Table 2.1 K-point sampling used for different crystal super cells

Super Cell	Kpoints Used
111	9x9x5
112	9x9x3
211	5x9x5
212	5x9x3
221	5x5x5

Table 2.2 Experimental volumes for crystal structures fixed constant during geometry optimizations

Model set	Volume of unit cell ($Å^3$)
$Re_1Si_1Al_1$	81.10
$Re_1Si_{0.75}Al_{1.25}$	81.40

For the analysis done by the Local Orbital Basis Suite Towards Electronic Reconstruction Package (LOBSTER), Integrated Crystal Orbital Hamilton Populations (ICOHP's) were computed by projecting the wave functions from VASP onto a localized basis

set of Slater-type atomic orbitals.[32][33] The average COHP energies for each model were taken up to the fermi level.

2.2 Energy Analysis

Using VASP, total static energies were calculated for each crystal super cell. Afterwards, a calculation allowing for the atoms in the unit cell to readjust spatially was done, then another static energy calculation with the optimized geometry was computed. This analysis was used to evaluate the favorability of mixed versus segregated states of $Re_1Si_1Al_1$. Another factor considered was the Ewald energy. This energy treats the energy of the crystal electrostatically. The approximation is assuming the material is an ideal metal with an electron 'sea' and cationic cores spread throughout. The Ewald Energy is compared with total energy to understand how favorable the mixing of aluminum and silicon is.

Another energy analysis technique is the computation of the ICOOP and ICOHP (integrated crystal orbital overlap population & integrated crystal orbital Hamilton population, respectively). This computation method was explained earlier in the introduction. All calculations were executed using the package LOBSTER. This type of energy analysis gives one an idea of the chemical covalent bonding taking place within the crystal. The plane wave basis set of wavefunctions are projected onto a slater type orbital localized basis set *via* LOBSTER. This basis set is shown in the Table 2.3 below.

So, overall there are several energy analysis techniques used in this research project: Total energy, Ewald Energy, as well as the ICOHP. These techniques were used to understand and explain Silicon doped Rhenium Aluminum compound's structure.

Table 2.3 Localized basis sets used for calculation of COHP

Atom	Slater type basis set projected onto
Rhenium	5d, 6s, 6p
Silicon	3s, 3p
Aluminum	3s, 3p

2.3 Band-structure Calculation

A bandstructure was computed *via* VASP for each artificial model. The KPOINTS for the bandstructures were generated using AFLOW.org (automatic FLOW for materials discovery).[34] Simply supplying AFLOW with the POSCAR (specifications of atomic positions) file from VASP and the kpath option selected will produce a suitable set of kpoint paths in order to compute a bandstructure (See Figure 2.2). An example of the KPOINTS used in the Brilloun Zone for $Re_1Si_1Al_1$ 111_1 bandstructure is shown below. In a bandstructure calculation, the k-points are sampled along a path of the Brilloun zone (reciprocal space of Wigner Seitz cell), for instance from Γ to M is shown below (along with several others). Γ typically represents the center of the Brilloun Zone. Bandstructure data files were exported with p4Vasp and plotted using the matplotlib library of python3.[35][36][37]

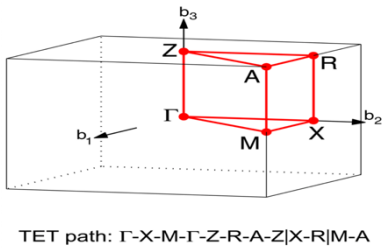

Figure 2.2 Brilloun Zone of 111_1 for $Re_1Si_1Al_1$ with kpaths for bandstructure calculation shown

2.4 Al-Rich Models

Not only have these types of methods been completed for $Re_1Si_1Al_1$, but also for $Re_1Si_{0.75}Al_{1.25}$ artificial model sets. These model sets follow a similar procedure of artificially segregating and mixing Aluminum and Silicon to various degrees. The study of these models will provide us answers why Al-rich compositions, such as $Re_1Si_{0.8}Al_{1.2}$, are different from $Re_1Si_1Al_1$ and do not have Al and Si segregation. Appendices A and B list all model structures created and used in this study.

CHAPTER 3 RESULTS & DISCUSSION

3.0 Overview

During this section of the thesis, outcomes of this computational study (and some experimental consideration) along with their rationalizations are included. The first section looks at $Re_1Si_1Al_1$ in detail whereas the next segment examines $Re_1Si_{0.75}Al_{1.25}$ in comparison with $Re_1Si_1Al_1$. These results will include analysis of energetics of model structures, band structures, charge density maps, as well as several other computational solid state topics of these materials.

3.1 Energy Analysis

As discussed previously in Chapter 2, several artificial models of $Re_1Si_1Al_1$ were created with constant Rhenium sites, while varying the segregation of Aluminum and Silicon to different degrees. Calculated energy terms of these model structures are displayed in the table below (Table 3.1), including the total energy, Ewald energy, and the total Integrated Crystal Hamilton Population (ICOHP). The energy terms of the supercell models were all normalized to the values per 1 × 1 × 1 unit cell. For instance, the total energy of a 1 × 1 × 2 supercell model needs to be divided by 2 to compare with the 1 × 1 × 1 unit cell models.

For better comparison, the energy terms of Model 111_2, which is the lowest in total energy, are used as references (set to 0 eV). And the energy terms of the other models are shown as relative values with respect to the references.

Table 3.1 Energy terms of $Re_1Si_1Al_1$ models including Total energy, Ewald energy, and total ICOHP. The models are sorted according to Ewald energy, which evaluates the degree of mixing between Al and Si.

Model ID	Total Energy (eV)	Ewald Energy (eV)	ICOHP (eV)
221_5	0.3907	-28.9629	0.7254
111_1	0.3899	-28.9425	0.6266
221_4	0.3054	-27.6146	0.4848
221_3	0.2334	-27.3552	0.3083
111_4	0.0411	-26.8385	0.6490
211_3	0.2143	-26.1692	0.2804
221_1	0.1808	-26.0628	0.3299
211_4	0.2118	-24.4898	0.1380
211_5	0.1916	-20.9597	0.0119
221_2	0.1299	-20.8864	0.4268
211_2	0.2372	-20.5831	0.2042
212_3	0.1784	-20.3932	0.2102
112_2	0.2841	-4.49596	0.5042
111_2	**0**	**0**	**0**
112_4	0.0969	1.871831	0.0069
112_1	0.6236	9.505486	0.6931
212_1	0.5118	39.38256	0.4736

3.2 Total Energy

Firstly, it can be seen from Table 3.1 that the lowest total energy occurs for Model 111_2, which means this should be the most stable among all model structures. Its crystal structure is displayed below (Figure 3.1). Where the unit cell is enclosed with the bold lines. The crystal structure is displayed as a 222 supercell for ease of comparison with other models. Al and Si atoms are segregated into alternating layers in Model 111_2. This is exactly the same as the experimental structure of $Re_1Si_1Al_1$ as determined by X-ray and neutron diffractions. Therefore, the computation matches the experimental results quite nicely.

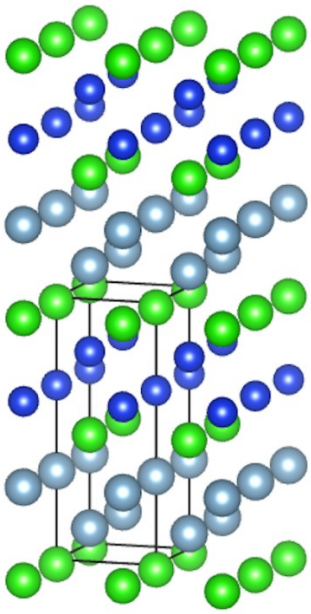

Figure 3.1 Lowest energy model $Re_1Si_1Al_1$ 111_2

3.3 Ewald Energy

Relative Ewald energies are displayed above in Table 3.1 as well. These energies are the electrostatic potential energy between homogeneous valence electron gas and the Re^{+7}, Al^{3+}, and Si^{4+} cations. They provide a convenient evaluation of the relative stabilities of a substance's polymorphs if the substance is close to an ideal metal. Evidently in Table 3.1, the most stable model, 111_2, does not have the lowest Ewald energy. Therefore, the stability of 111_2 cannot be rationalized with this simplistic potential energy between cations and homogeneous valence electron gas, which also indicates that $Re_1Si_1Al_1$ must deviate significantly from an ideal metal. Meanwhile, Ewald energy does show a clear pattern with respect to the segregation between Al and Si atoms. Displayed below in Figure 3.2 are 4 representative $Re_1Si_1Al_1$ models from Table 3.1 with their relative Ewald Energies. It is clear that the models with lower Ewald energies typically have more mixing between Al and Si whereas the models with more segregation

between Al and Si have much higher Ewald energies. Therefore, had $Re_1Si_1Al_1$ been close to an ideal metal, Al and Si atoms should not be segregated but mixed. This is easily understandable. When $Re_1Si_1Al_1$ is approximated as an ideal metal, Re^{+7}, Al^{3+}, and Si^{4+} cations plus homogeneous electron gas, Si^{+4} ions would prefer to be surrounded by Al^{+3} ions rather than themselves.

Therefore because of this pattern in Ewald energy, it can be used to quantify the degree of mixing between Al and Si atoms. And the models in Table 3.1 are sorted according to Ewald energy. So even though Ewald energy is not the determining factor here, it does demonstrate that Al and Si cannot be infinitely segregated as this will cause too high Ewald energy and destabilize the structure.

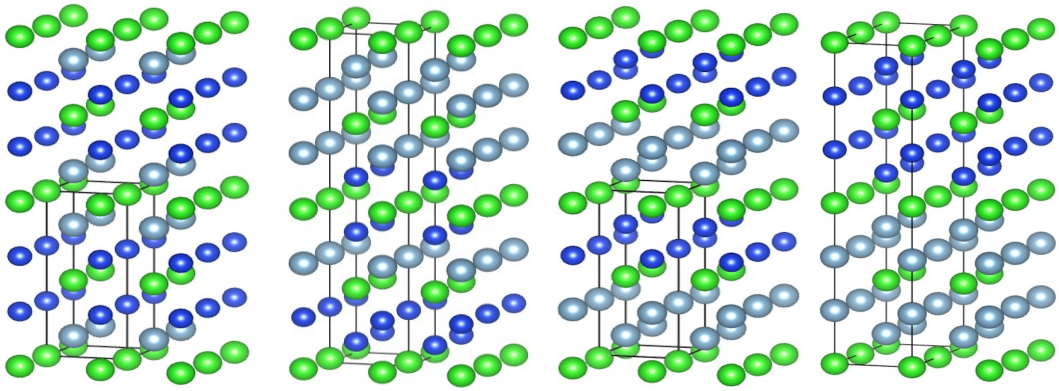

111 1	112 2	111 2	212 1
-28.96 eV	-4.50 eV	0 eV	39.38 eV

Figure 3.2 Selected models for comparison of Ewald Energy to show mixing and segregation of Aluminum and Silicon

3.4 Total ICOHP

Integrated Crystal Overlap Hamilton Population calculates the energy lowered by bonding interactions between atoms. Therefore, it semi-quantitatively evaluates the bonding energy and bond strength. The lower the ICOHP is, the stronger the bonding is. The total ICOHP in Table

3.1 evaluates the overall bonding from all bonds per 1 × 1 × 1 unit cell. It is shown that the most stable model, Model 111_2 has also the lowest ICOHP, so it has the strongest bonding among all model structures. This suggests that chemical bonding plays a major role in determining the arrangement of Al and Si atoms. The experimentally characterized arrangement, as in Model 111_2 affords the strongest overall bonding. Besides the total ICOHP, this analysis can be taken further by analyzing the partial ICOHP for different types of bonds, which will reveal more details about why Model 111_2 affords the strongest overall bonding.

3.5 Partial ICOHP of Specific Bonds

Displayed in Table 3.2 are the values of ICOHP for each of the three types of bonds, Re-Si, Re-Al, and Al/Al-Si/Si. The values listed for each type of bonds include their ICOHP per 1 × 1 × 1 unit cell as well as the average ICOHP per bond. Because the number of each type of bond per cell is equal (10 bonds per cell for each type), the ICOHP/bond and ICOHP/cell exhibit the same pattern. Firstly, it can be seen from Table 3.2 that the Al-Al, Si-Si, and Al-Si bonding is much weaker (less negative ICOHP) in comparison to Re-Si, and Re-Al. Between Re-Si and Re-Al, Re-Si is stronger (more negative ICOHP). This is the case for all models. Comparing the ICOHP across the models, Re-Si and Re-Al exhibit opposite trends – a model with lower Re-Si ICOHP is always higher in Re-Al ICOHP. This indicates that Re-Si and Re-Al are competitive. Optimizing Re-Si means sacrificing Re-Al and vice versa. Re-Si bonding is stronger than Re-Al, Re-Si wins the competition. It is beneficial to optimize Re-Si bonding and sacrifice Re-Al. This is demonstrated by the same trend between Re-Si ICOHP and total ICOHP – a model with lower Re-Si ICOHP is also lower in total ICOHP. Among all models, 111_2, which has the lowest total energy (Table 3.1) and the lowest total ICOHP (Table 3.2), has also the lowest Re-Si ICOHP.

Therefore, the best overall bonding and relative stability of Model 111_2 can be attributed to the fact that it affords the optimum Re-Si bonding.

Table 3.2 Total ICOHP and Partial ICOHP values of each bond type in selected models.

Model	Re-Si (10 bonds per 1×1×1 cell)		Re-Al (10 bonds per 1×1×1 cell)		Al/Si-Al/Si (10 bonds per 1×1×1 cell)		Total
	ICOHP/ bond (eV)	ICOHP/ cell (eV)	ICOHP/ bond (eV)	ICOHP/ cell (eV)	ICOHP/ bond (eV)	ICOHP/ cell (eV)	ICOHP/ cell (eV)
111_1	-2.89	-28.87	-2.67	-26.65	-1.49	-14.90	-70.41
221_4	-2.94	-29.45	-2.63	-26.35	-1.42	-14.16	-69.95
221_3	-2.99	-29.91	-2.63	-26.26	-1.43	-14.34	-70.51
111_4	-2.98	-29.80	-2.59	-25.87	-1.47	-14.72	-70.39
211_3	-2.99	-29.94	-2.61	-26.10	-1.47	-14.73	-70.76
221_1	-3.01	-30.05	-2.60	-26.04	-1.46	-14.63	-70.72
211_4	-3.05	-30.50	-2.58	-25.80	-1.46	-14.60	-70.90
211_5	-3.10	-31.00	-2.54	-25.43	-1.46	-14.61	-71.03
221_2	-3.04	-30.43	-2.57	-25.65	-1.45	-14.48	-70.57
211_2	-3.06	-30.60	-2.57	-25.66	-1.43	-14.35	-70.60
212_3	-3.05	-30.54	-2.57	-25.67	-1.46	-14.63	-70.83
112_2	-3.06	-30.64	-2.52	-25.19	-1.47	-14.71	-70.54
111_2	**-3.26**	**-32.59**	**-2.41**	**-24.11**	**-1.43**	**-14.35**	**-71.04**
112_4	-3.15	-31.53	-2.50	-24.99	-1.45	-14.52	-71.03
112_1	-2.99	-29.92	-2.55	-25.51	-1.49	-14.92	-70.35
212_1	-3.23	-32.25	-2.39	-23.90	-1.44	-14.42	-70.57

A close examination of the crystal structures reveals why Model 111_2 affords the Re-Si bonding. Figure 3.3 shows the comparison of Re-Si bonds in three model structures. The Re-Si bonds in a unit cell can be categorized into diagonal Re-Si and vertical Re-Si. To strengthen (shorten) the diagonal Re-Si, the unit cell needs to be elongated to shrink the *a* and *b*, and the Re

and Si atoms should also be moved up and down in the *c* direction as indicated by the black arrows in Figure 3.3. In models whose Al and Si atoms are not segregated, such as 111_1 and 111_4 in Figure 3.3, all these shortening in the diagonal Re-Si elongate the vertical Re-Si. So strengthening the former would sacrifice the latter. However, in 111_2, when Al and Si are segregated, diagonal and vertical Re-Si can be shortened simultaneously. This is why it affords the optimum Re-Si bonding.

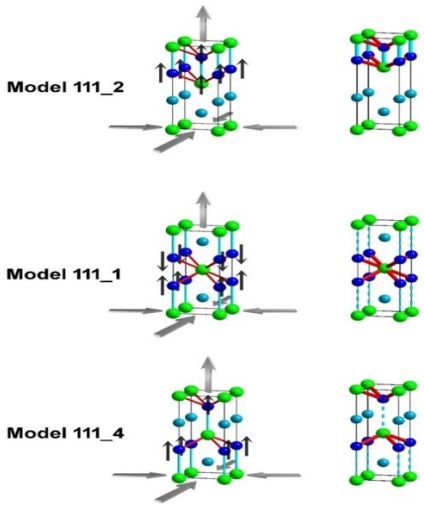

Figure 3.3 Comparison of Re-Si bonds in 3 model structures. There are diagonal (red) and vertical (light blue) Re-Si bonds shown. The gray arrows indicate the elongation of unit cells and the black arrows show the movement of atoms. Only 111_2 allows for the shortening of both diagonal and vertical Re-Si bonds. For the other two models, shortening the diagonal Re-Si bonds elongates the vertical ones.

3.6 Band Structure

Band structures were computed for all models and all are shown in the Appendix. Below, in Figure 3.4, the band structures of 111_1 and 111_2 are shown. The structures of these two

models are both shown in Figure 3.2. Al and Si are segregated in 111_2 but mixed in 111_1. Firstly, 111_2 clearly possesses a distinct bandgap at the Fermi level (E_F) whereas 111_1 does not. If we refer to the band structures for all the model structures (Appendix), the ones with lower total energy always exhibit more evident band gaps at E_F. Such an evident band gap at E_F in a solid is analogous as a large energy gap between HOMO and LUMO in a molecule and usually indicates a better electronic stabilization. In order to analyze why the band gaps are more evident in the more stable model structures, we focus on and compare the 4 bands in the vicinity of E_F, Bands 13 – 16 (highlighted with red boxes), in both 111_2 and 111_1. In 111_2, Bands 13 and 14 are degenerate and below E_F and Bands 15 and 16 are degenerate and above E_F at Γ point. By comparison, in 111_1, Band 13 is below E_F while Bands 14 – 16 are all above. Bands 14 and 15 are crossing E_F to the left of Γ point. To see what makes this difference in band structure between 111_2 and 111_1 partial charge density maps were generated at the Γ point for Bands 13 – 16 (Figure 3.5). These maps show where valence electrons are localized at. As shown below in Figure 3.5, each of these charge densities demonstrate certain bonding characteristics of the crystal structures. For 111_2, the degenerate Bands 13 and 14 have identical partial charge densities, in which valence electrons are concentrated between Re and Si, as well as Re and Al. So they both exhibit Re-Si and Re-Al bonding simultaneously. The degenerate Bands 15 and 16 are also identical and show Al-Al and Si-Si bonding. For 111_1, Bands 14 and 15 are about Al-Si bonding, which are counterparts of Bands 15 and 16 in 111_2. Bands 13 and 16 are about bonding of Re with Al and Si so they are counterparts of Band 13 and 14 in 111_2. But apparently, due to the different arrangement of Al and Si, Re-Si and Re-Al do not occur simultaneously. Band 13 of 111_1 is pure Re-Si and Band 16 is pure Re-Al. They are not identical and not degenerate. Because Al's valence orbitals are higher in energy than Si's valence

orbitals, the Re-Al bonding band (Band 16) has much higher energy and is raised above E_F, which closes the band gap. The code to generate these band structures is shown in Appendix C as well as a compilation of all band structures in Appendices D and E.

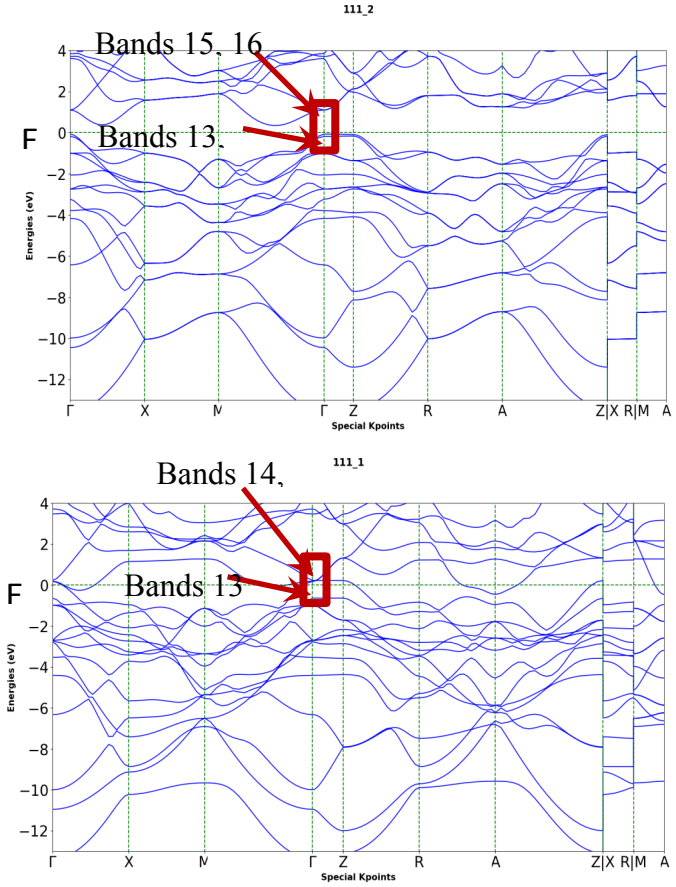

Figure 3.4 Computed band structure of $Re_1Si_1Al_1$ 111_2 & 111_1 plotted with python3

3.7 Concluding Remarks

Overall, as determined experimentally, Al and Si atoms are segregated in $Re_1Si_1Al_1$. By way of this computational study, several factors appear to be at play in segregating Al and Si.

First of all, the experimentally determined model has the lowest total energy when compared to models of varying Si and Al mixing/segregation. This shows that our quantum mechanical calculations reproduce the experimental observations. This total energetic stability of the experimental structure appears to be correlated directly to its most stable overall chemical bonding, viz. the lowest total ICOHP. Furthermore, the most stable overall bonding can be attributed the most optimum Re-Si bonding, which is the most favorable among all bond types. The reason why the experimental structure affords the optimum Re-Si bonding is because, when Al and Si are segregated, both diagonal and vertical Re-Si bonds can be shortened (strengthened) simultaneously whereas, in the Al/Si mixed models, strengthening the diagonal Re-Si weakens the vertical ones. Band structure and partial density maps rationalize the advantage of the experimental structure from another angle – band gap opening, which is a sign of electronic stabilization. The Ewald energy analyses shows the disadvantage of segregating Al and Si and explains why they are not segregated even further than the experimental structure – further segregation would raise the Ewald energy too high and destabilize the structure.

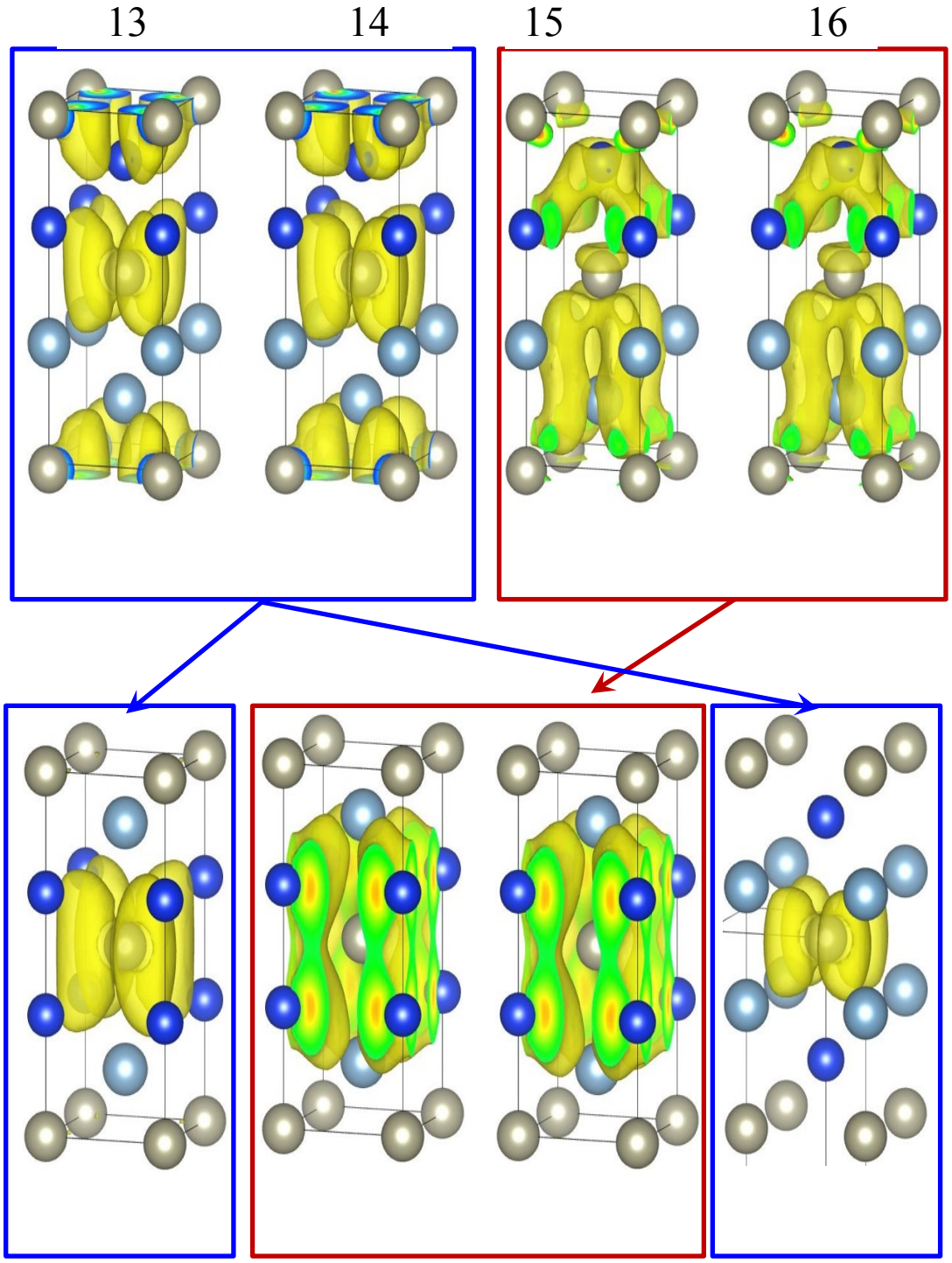

Figure 3.5 Partial charge densities of 111 model 1 & 2 at the Γ point for 2 bands above and below the fermi level

CHAPTER 4 RESULTS & DISCUSSION OF ALUMINUM RICH MODELS

4.0 $Re_1Si_{0.75}Al_{1.25}$ Models

Artificial models of several $Re_1Si_{0.75}Al_{1.25}$ were also established and computed. In this next section of the results and discussion these models will be looked at in a similar fashion too as well as being compared with $Re_1Si_1Al_1$ models. The reason to study $Re_1Si_{0.75}Al_{1.25}$ is that, experimentally, it was found that, in a range of $Re_1Si_{0.8\text{-}0.7}Al_{1.2\text{-}1.3}$, the crystal structure formed is body centered, and, unlike in $Re_1Si_1Al_1$, Si and Al atoms are not segregated any more but statistically share the same crystallographic sites. This section seeks to explain why Si and Al behave differently when Al gets richer in the composition.

4.1 Energy Analysis

Similarly to $Re_1Si_1Al_1$ models, several artificial models were built. All previous calculations were also completed for this model set. Below in Table 4.1 are the total energy, Ewald energy, and total ICOHP values displayed for several selected models all relative against the lowest total energy model (221_2). Firstly, note that 221_2 possesses the lowest total energy. And there are two other models, 221_3 and 211_1, whose total energies are virtually equal to 221_2, only 8 and 4 meV higher. In all these 3 models, Si and Al are still segregated in a way similar to the $Re_1Si_1Al_1$ 111_2 model (the lowest-energy and experimental model of $Re_1Si_1Al_1$). Figure 4.1 compares these three models with $Re_1Si_1Al_1$ 111_2. They can all be obtained by replacing 1/4 of the Si with Al (in three different ways) from $Re_1Si_1Al_1$ 111_2. Therefore, Al and Si segregation is still energetically favorable for $Re_1Si_{0.75}Al_{1.25}$.

Table 4.1 Calculations of total relative energy, relative Ewald energy, and relative total ICOHP values for $Re_1Si_{0.75}Al_{1.25}$ artificial models.

Model ID	Total Energy (eV)	Ewald Energy (eV)	ICOHP (eV)
221_1	0.2865	-33.5648	0.1232
222-2	0.2612	-31.0111	0.0997
211_2	0.2238	-29.0657	-0.0165
222-3	0.2426	-28.9705	0.1234
212_4	0.1385	-28.5657	0.0259
222-5	0.2714	-27.4664	0.1709
211_4	0.1695	-21.7892	-0.1865
212_2	0.2118	-21.2038	-0.0567
221_4	0.1269	-18.2852	0.0511
112_3	0.0761	-17.1058	-0.0836
212_3	0.1051	-8.1287	-0.1186
222-4	0.0527	-5.5241	0.0282
112_5	0.4408	-3.9539	-0.0801
221_2	**0.0000**	**0.0000**	**0.0000**
221_3	0.0076	0.0174	-0.0349
211_1	0.0042	0.0462	-0.1294
112_4	0.1383	56.5636	-0.2714
212_5	0.4716	59.0014	-19.4251
112_2	0.5863	62.2723	-0.3035

4.2 Total Energy

Firstly, note that 221_2 possesses the lowest total energy. And there are two other models, 221_3 and 211_1, whose total energies are virtually equal to 221_2, only 8 and 4 meV higher. In

all these 3 models, Si and Al are still segregated in a way similar to the $Re_1Si_1Al_1$ 111_2 model (the lowest-energy and experimental model of $Re_1Si_1Al_1$). Figure 4.1 compares these three models with $Re_1Si_1Al_1$ 111_2. They can all be obtained by replacing 1/4 of the Si with Al (in three different ways) from $Re_1Si_1Al_1$ 111_2. Therefore, Al and Si segregation is still energetically favorable for $Re_1Si_{0.75}Al_{1.25}$.

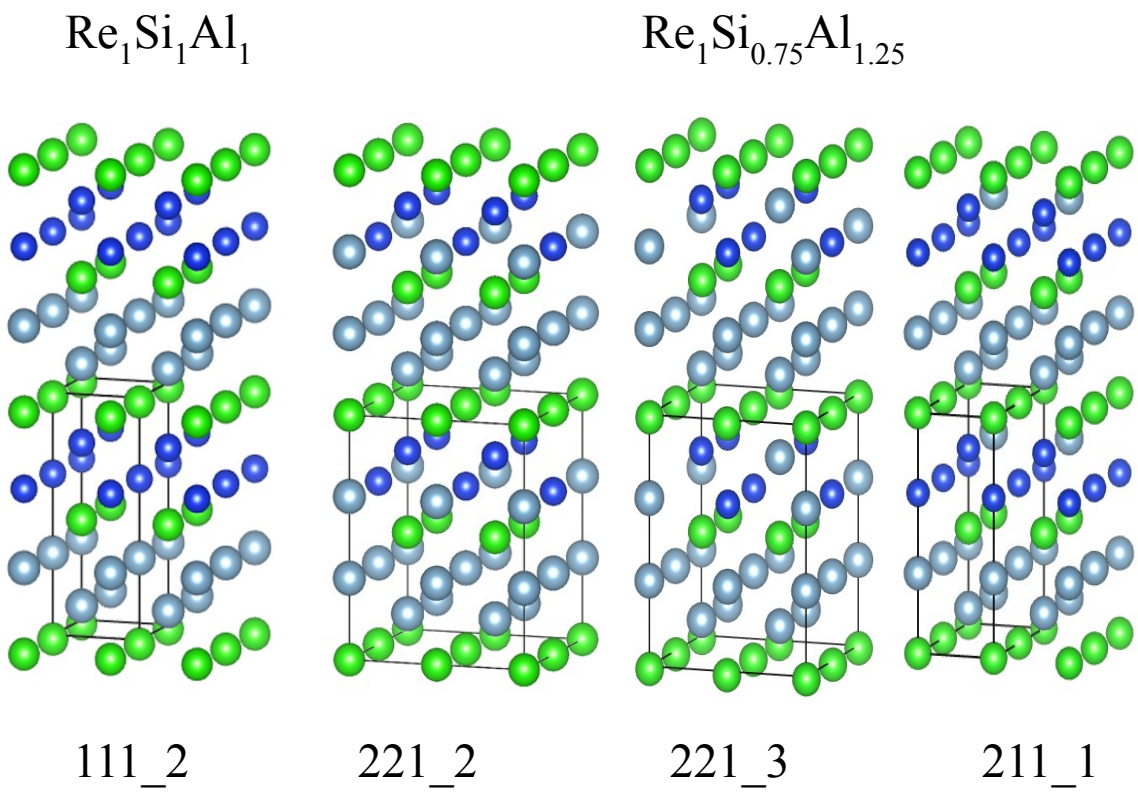

Figure 4.1 Comparison between $Re_1Si_1Al_1$ 111_2 and $Re_1Si_{0.75}Al_{1.25}$ 221_2, 221_3, and 211_1.

Meanwhile, we can also see that, even though 221_2, 221_3, and 211_1 are the most stable, their advantage is not so significant. The synthetic temperature for these compounds is 1000 °C, which is sufficient to overcome an energy difference of 0.086 eV. In Table 3.3, there are at least

three models whose total energies are within 0.086 eV higher than 221_2, including 211_5 (0.038 eV), 112_1 (0.076 eV), and 222_4 (0.053 eV). The structures of these 3 models are shown in Figure 4.2. Apparently, Al and Si are not segregated in these models.

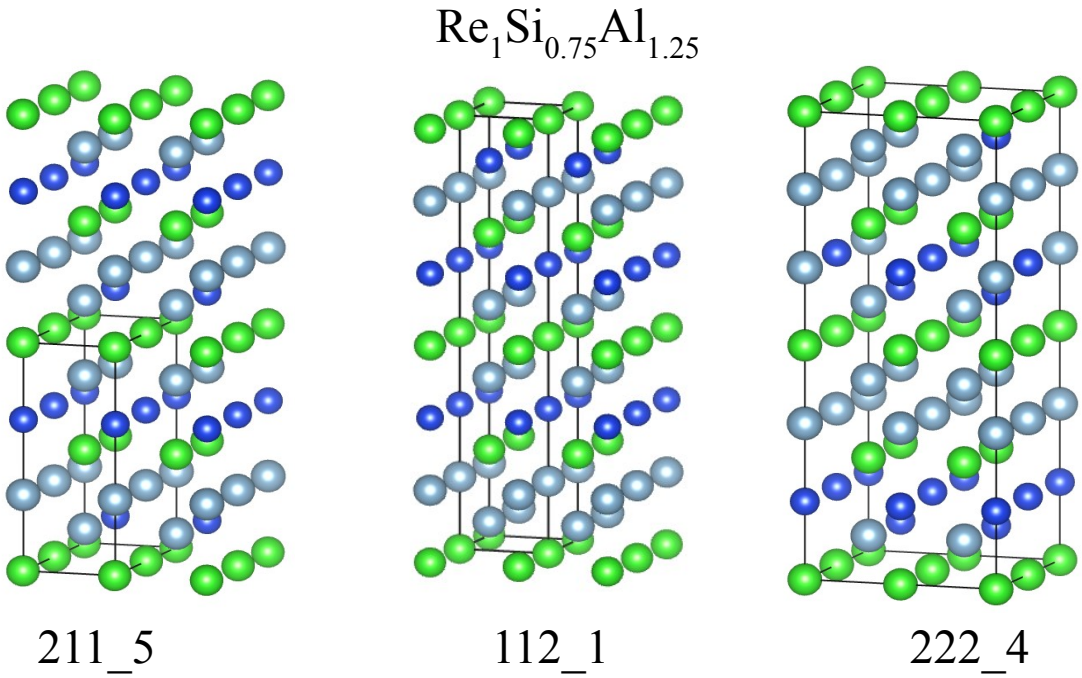

Figure 4.2 The structures of $Re_1Si_{0.75}Al_{1.25}$ 211_5, 112_1, and 222_4.

4.3 Ewald Energy

Consistently with the previous $Re_1Si_1Al_1$ models, Ewald energies are lowest with the most mixed aluminum and highest with the most segregated. Because of this, once again, these values were taken to be a quantitative measure of how 'mixed' a crystal structure was and the models in Table 4.1 are sorted according to Ewald energy. In Figure 4.3 below, four different models are displayed to illustrate this point. Energies are displayed, as before, relative to the lowest total energy model (221_2).

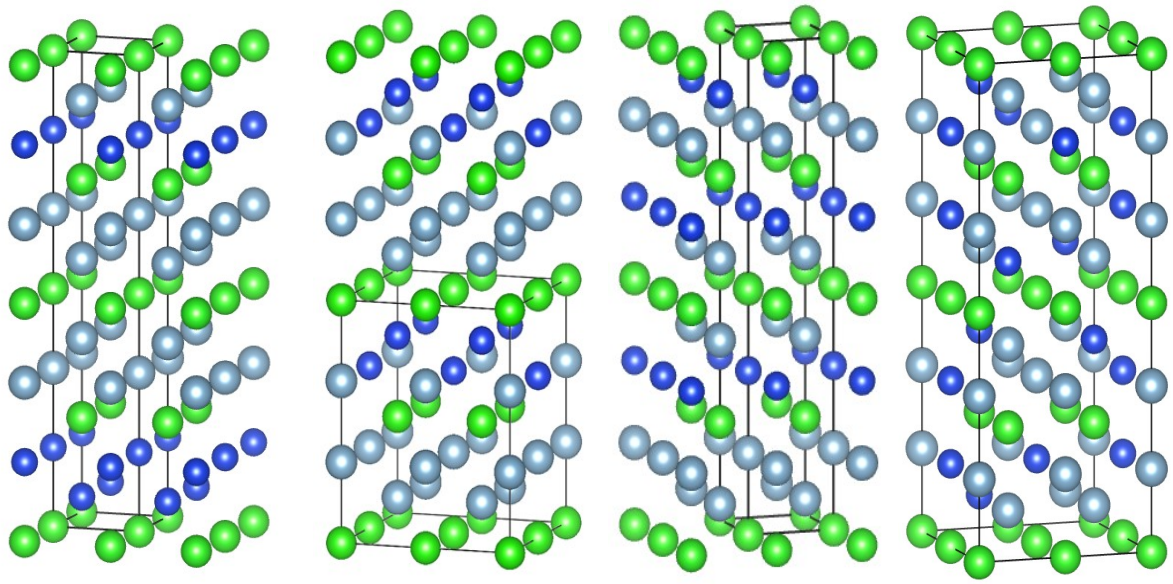

Figure 4.3. Four selected $Re_1Si_{0.75}Al_{1.25}$ models for comparison of Ewald energy and qualitative silicon and aluminum segregation

4.4 Total ICOHP

Observing the previous comprehensive Table 4.1, it is seen that the three lowest total energy models no longer possesses the most negative total ICOHP values. This suggests that total energy and bonding are not directly related as in $Re_1Si_1Al_1$ models. So for $Re_1Si_{0.75}Al_{1.25}$, the segregation of Al and Si does not lead to the strongest overall bonding any more. To see why this is the case, individual contributions of Re-Si, Re-Al, and Si/Si-Al/Al partial ICOHPs are examined in the next section.

4.5 Partial ICOHP of Specific Bonds

Table 4.2 lists the partial ICOHP values for Re-Si, Re-Al, and Al/Si-Al/Si bonds along with the total ICOHP. For each type of bonds, the partial ICOHP values are listed both as average per bond and as sum per 1 × 1 × 1 unit cell.

When we compare the average ICOHP per bond, we can observe some features similar to the partial ICOHP values in $Re_1Si_1Al_1$ models (Table 3.2). Firstly, a Re-Si bond is still stronger than a Re-Al bond or an Al/Si-Al/Si bond. The average Re-Si ICOHP's range from -2.9 to -3.2 eV/bond while Re-Al has only -2.5 to -2.6 eV/bond and Al/Si-Al/Si has only -1.4 to -1.7 eV/bond. Secondly, the segregation of Al and Si still makes the optimum Re-Si bonding. The three segregated (lowest-energy) models, 221_2, 221_3, and 211_1, have the second most negative average Re-Si ICOHP per bond, -3.19 eV/bond. The most negative average Re-Si ICOHP occurs in 112_4 (Figure 3.8), in which Si and Al are even more segregated and exhibits a very high Ewald energy. Thirdly, Re-Si and Re-Al still exhibit opposite trends – a model with more negative Re-Si ICOHP is always less negative in Re-Al ICOHP. Optimizing one means sacrificing the other.

However, when we compare the sum of ICOHP per 1 × 1 × 1 unit cell for each type of bonds, we see clear dissimilarity between $Re_1Si_{0.75}Al_{1.25}$ and $Re_1Si_1Al_1$ models. Firstly, unlike the $Re_1Si_1Al_1$ models, the number of each type of bonds is not equal. There are 7.5 Re-Si, 12.5 Re-Al, and 10 Al/Si-Al/Si bonds per 1 × 1 × 1 unit cell. So even though Re-Si is the strongest per bond, Re-Al bonding wins by number. The Re-Si ICOHP/cell ranges from -22 to 24 eV/cell while the Re-Al ICOHP/cell varies from -31 to -32 eV/cell. It is Re-Al that contributes the most to the total ICOHP/cell.

So like $Re_1Si_1Al_1$, the Al and Si segregation still optimizes Re-Si bonding. However, unlike $Re_1Si_1Al_1$, Re-Si bonding is not the dominant contributor to the total bonding in $Re_1Si_{0.75}Al_{1.25}$ because there are many fewer Re-Si than Re-Al. So optimizing Re-Si does not lead to the strongest total bonding. This explains why the Al and Si segregated models do not have the most negative total ICOHP and why Al and Si segregation is less favorable in $Re_1Si_{0.75}Al_{1.25}$.

Table 4.2 Specific ICOHP value / bond of $Re_1Si_{0.75}Al_{1.25}$ models along with total ICOHP/ cell for comparison

Model	Re-Si (7.5 bonds per 1×1×1 cell)		Re-Al (12.5 bonds per 1×1×1 cell)		Al/Si-Al/Si (10 bonds per 1×1×1 cell)		Total
	ICOHP/bond (eV)	ICOHP/cell (eV)	ICOHP/bond (eV)	ICOHP/cell (eV)	ICOHP/bond (eV)	ICOHP/cell (eV)	ICOHP/cell (eV)
112_1	-3.03	-22.69	-2.59	-32.37	-1.75	-17.47	-145.06
112_2	-3.14	-23.56	-2.54	-31.75	-1.46	-14.55	-139.71
112_3	-3.02	-22.68	-2.59	-32.33	-1.75	-17.46	-144.94
112_4	-3.22	-24.14	-2.51	-31.36	-1.43	-14.33	-139.66
112_5	-2.93	-22.00	-2.63	-32.87	-1.40	-13.99	-137.70
211_1	-3.19	-23.94	-2.51	-31.34	-1.43	-14.29	-139.13
211_2	-3.02	-22.61	-2.59	-32.44	-1.42	-14.20	-138.50
211_3	-2.95	-22.10	-2.62	-32.70	-1.36	-13.57	-136.73
211_4	-3.09	-23.15	-2.56	-32.04	-1.41	-14.14	-138.67
211_5	-3.01	-22.55	-2.59	-32.41	-1.78	-17.77	-145.45
212_1	-2.95	-22.09	-2.61	-32.67	-1.36	-13.61	-136.73
212_2	-3.05	-22.90	-2.58	-32.19	-1.42	-14.16	-138.49
212_3	-3.10	-23.25	-2.55	-31.91	-1.41	-14.14	-138.60
212_4	-3.01	-22.56	-2.59	-32.40	-1.42	-14.15	-138.23
221_1	-2.97	-22.30	-2.61	-32.61	-1.40	-14.02	-137.87
221_2	-3.19	-23.91	-2.50	-31.25	-1.43	-14.28	-138.89
221_3	-3.19	-23.95	-2.50	-31.28	-1.42	-14.24	-138.92
221_4	-3.08	-23.12	-2.55	-31.94	-1.43	-14.26	-138.63
221_5	-3.09	-23.16	-2.56	-31.94	-1.42	-14.18	-138.56
221_6	-3.02	-22.66	-2.58	-32.31	-1.41	-14.09	-138.12
222-1	-2.94	-22.05	-2.60	-32.53	-1.36	-13.59	-136.33

4.6 Band Structure

In the case of $Re_1Si_1Al_1$, as discussed in Chapter 3.6, the model structures with Al and Si segregation exhibit more evident band gaps at the Fermi level. This is analogous to a larger HOMO-LUMO gap and indicates electronic stabilization. For comparison, the band structures of $Re_1Si_{0.75}Al_{1.25}$ Models 211_1 and 211_3 are shown below in Figure 4.4. Model 211_1 is one of the Si/Al segregated models (Figure 4.2) with the lowest total energy (Table 4.1), while in Model 211_3 (Appendix), Al and Si are more mixed. Figure 4.4 shows that, Si/Al segregated Model 211_1 possesses an evident band gap while Si/Al mixed 211_3 has only a pseudogap. This is consistent with the observations in $Re_1Si_1Al_1$. However, there is also a very significant difference between $Re_1Si_{0.75}Al_{1.25}$ and $Re_1Si_1Al_1$. The band gap/pseudogap occurs at the Fermi level in $Re_1Si_1Al_1$ but, in $Re_1Si_{0.75}Al_{1.25}$, it occurs about 1 eV above the Fermi level. This is because, from $Re_1Si_1Al_1$ to $Re_1Si_{0.75}Al_{1.25}$, the number of valence electrons decreases from 14 e^-/f.u. to 13.75 e^-/f.u. so fewer bands are occupied and the Fermi level drops.

Therefore, just like in $Re_1Si_1Al_1$, Al and Si segregation also leads to a more evident band gap for $Re_1Si_{0.75}Al_{1.25}$. However, unlike in $Re_1Si_1Al_1$, the gap is 1 eV above E_F. The bands immediately below and above the gap are not "HOMO" and "LUMO" any more but are all unoccupied. The gap opening occurring for these empty virtual states will not lead to electronic stabilization.

4.7 Concluding Remarks

Overall, Aluminum rich models have been computed for comparison with the $Re_1Si_1Al_1$ model sets. Firstly it is seen that the total lowest energy model of the Aluminum rich case corresponds to similar Aluminum and Silicon segregation with the $Re_1Si_1Al_1$ case. Bonding and

band structure analyses reveal that the factors that favor Al and Si segregation are still present in $Re_1Si_{0.75}Al_{1.25}$ but they are not the structural determining factor any more.

Firstly, Al and Si segregation still optimizes Re-Si bonding. However, it is seen that the $Re_1Si_{0.75}Al_{1.25}$ models have clearly much more Re-Al rather than Re-Si bonding. This means that Re-Si bonding energy is no longer as influential as it was for the previous case for contributing to the overall bonding and total energy of the crystal.

Lastly, the band structures for the Aluminum rich case still show band gap opening upon Al and Si segregation, but the gap opening occurs with unoccupied virtual bands, which does not affect electronic energy and will not lead to electronic stabilization.

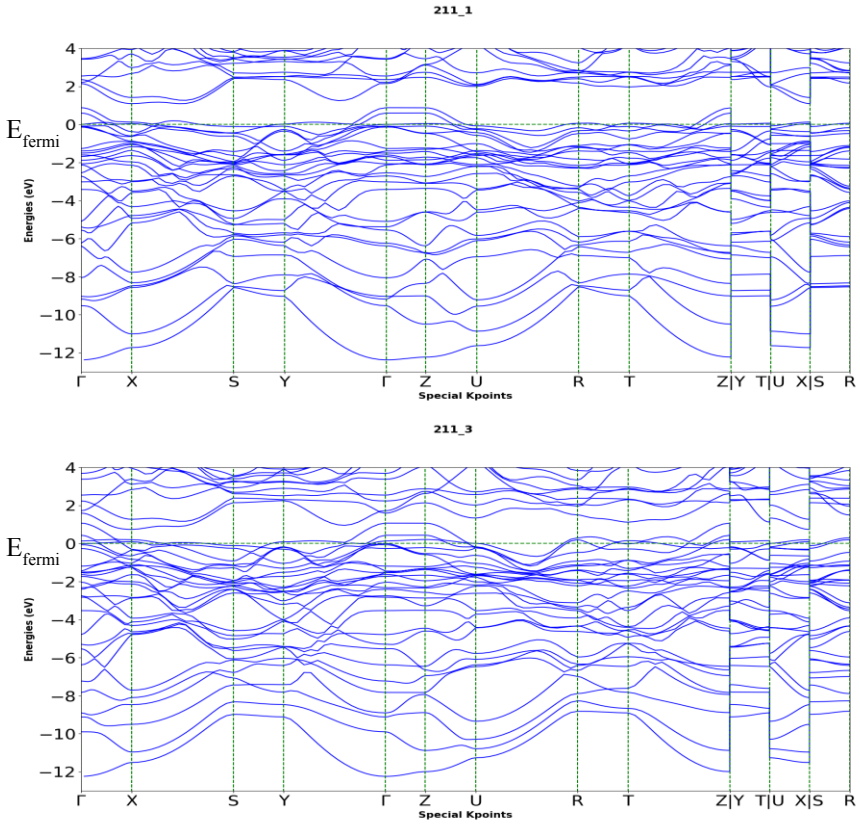

Figure 4.4. Top bandstructure 211_1 bottom 211_3

Considering these observations in $Re_1Si_{0.75}Al_{1.25}$, even though the Al/Si segregated models still have the lowest total energy, their energetic advantage is not so significant anymore. There are several Al/Si mixed models that are only high by tens of meV in total energy. During the high temperature synthesis, $Re_1Si_{0.75}Al_{1.25}$ can overcome these relatively small energy differences to form a more disordered (entropically favored) structure.

REFERENCES

[1] Charge Density and Structural Characterization of Thermoelectric Materials. *Materials Research Foundations***2016**.

[2] G. Kresse; J. Hafner. Ab initio molecular dynamics for liquid metals. Phys. Rev. B. **1993**, 47:558,

[3] Caton, J. A. Maximum Efficiencies for Internal Combustion Engines: Thermodynamic Limitations. *International Journal of Engine Research***2017**, *19*(10), 1005–1023.

[4] Montzka, S. A.; Dutton, G. S.; Yu, P.; Ray, E.; Portmann, R. W.; Daniel, J. S.; Kuijpers, L.; Hall, B. D.; Mondeel, D.; Siso, C.; Nance, J. D.; Rigby, M.; Manning, A. J.; Hu, L.;

[5] Moore, F.; Miller, B. R.; Elkins, J. W. An Unexpected and Persistent Increase in Global Emissions of Ozone-Depleting CFC-11. *Nature***2018**, *557*(7705), 413–417.

[6] Pei, Y.; Lalonde, A.; Iwanaga, S.; Snyder, G. J. High Thermoelectric Figure of Merit in Heavy Hole Dominated PbTe. *Energy & Environmental Science***201a1**, *4*(6), 2085.

[7] Anno, Y.; Imakita, Y.; Takei, K.; Akita, S.; Arie, T. Enhancement of Graphene Thermoelectric Performance through Defect Engineering. *2D Materials***2017**, *4*(2), 025019.

[8] Ha, J. U.; Cho, J.; Yoon, S.; Jang, M. S.; Hassan, S. Z.; Kang, M. G.; Chung, D. S. Polyvinyl Alcohol Covalently Grafted CNT for Free-Standing, Flexible, and High-Performance Thermoelectric Generator Film. *Nanotechnology***2019**, *30*(14).

[9] Snyder, G. J.; Snyder, A. H. Figure of Merit ZT of a Thermoelectric Device Defined from Materials Properties. *Energy & Environmental Science***2017**, *10*(11), 2280–2283.

[10] G. Kresse; J. Furthmüller. Efficiency of ab-initio total energy calculations for metals and semiconductors using a plane-wave basis set. Comput. Mat. Sci. **1996**, 6:15

[11] Wang, F.; Veremchuk, I.; Lidin, S. Tuning Crystal Structures and Thermoelectric Properties through Al Doping in ReSi1.75. *European Journal of Inorganic Chemistry* **2016**, *2017*(1), 47–55.

[12] Sakamaki, Y.; Kuwabara, K.; Jiajun, G.; Inui, H.; Yamaguchi, M.; Yamamoto, A.; Obara, H. Crystal Structure and Thermoelectric Properties of $ReSi_{1.75}$Based Silicides. *Materials Science Forum***2003**, *426-432*, 1777–1782.

[13] Yannello, V. J.; Fredrickson, D. C. *Inorganic Chemistry***2015**, *54*(23), 11385.

[14] Cox, H.; MacQuarrie, D. A.; Simon, J. D. *Physical chemistry: a molecular approach*; Univ. Science Books: Sausalito, CA, **1997**.

[15] Dronskowski, R. *Computational chemistry of solid state materials: a guide for materials scientists, chemists, physicists and others*; Wiley-VCH: Weinheim, **2007**.

[16] Hohenberg, P.; Kohn, W. Inhomogeneous Electron Gas. *Physical Review* **1964**, *136*(3B).

[17] Kohn, W.; Sham, L. J. Self-Consistent Equations Including Exchange and Correlation Effects. *Physical Review***1965**, *140*(4A).

[18] Sholl, D.; Steckel, J. A.; Sholl. *Density Functional Theory: a Practical Introduction*; Wiley: Somerset, **2011**.

[19] Kittel, C. *Introduction to solid state physics*; Wiley: Hoboken, NJ.

[20] Monkhorst, H. J.; Pack, J. D. Special Points for Brillouin-Zone Integrations. *Physical Review B* **1976**, *13*(12), 5188–5192.

[21] P. E. Blochl, Projector augmented-wave method. Phys. Rev. B, **1994**, 50:17953,

[22] The original COHP definition: R. Dronskowski, P. E. Blöchl, *J. Phys. Chem.* **1993**, *97*, 8617–8624.

[23] The projected COHP definition: V. L. Deringer, A. L. Tchougréeff, R. Dronskow- ski, *J. Phys. Chem. A* **2011**, *115*, 5461–5466.

[24] Mulliken, R. S. Electronic Population Analysis on LCAO–MO Molecular Wave Functions. I. *The Journal of Chemical Physics***1955**, *23*(10), 1833–1840.

[25] Hoffmann, R. *Solids and surfaces: a chemists view of bonding*; VCH Publishers: New York, NY, **1988**.

[26] Miller, G. J. The "Coloring Problem" in Solids: How It Affects Structure, Composition and Properties. *European Journal of Inorganic Chemistry* **1998,** 523-536.

[27] Momma, K.; Izumi, F. VESTA: a Three-Dimensional Visualization System for Electronic and Structural Analysis. *Journal of Applied Crystallography***2008**, *41*(3), 653–658.

[28] G. Kresse ;J. Hafner. Ab initio molecular-dynamics simulation of the liquid-metal-amorphous-semiconductor transition in germanium. Phys. Rev. B. **1994** 49:14251,.

[29] G. Kresse ; J. Furthmüller. Efficient iterative schemes for ab initio total-energy calculations using a plane-wave basis set. Phys. Rev. B. **1996**, 54:11169,

[30] G. Kresse ;D. Joubert. From ultrasoft pseudopotentials to the projector augmented-wave method. Phys. Rev. B. **1999**, 59:1758

[31] Pei, Y.; Lalonde, A.; Iwanaga, S.; Snyder, G. J. High Thermoelectric Figure of Merit in Heavy Hole Dominated PbTe. *Energy & Environmental Science***2011**, *4*(6), 2085.

[32] The mathematical apparatus and the framework on which LOBSTER is built: S. Maintz, V. L. Deringer, A. L. Tchougréeff, R. Dronskowski, *J. Comput. Chem.* **2013**, *34*, 2557–2567.

[33] LOBSTER 2.0.0 and its nuts and bolts: S. Maintz, V. L. Deringer, A. L. Tchougréeff, R. Dronskowski, *J. Comput. Chem.* **2016**, *37*, 1030–1035.

[34] Curtarolo, S.; Setyawan, W.; Hart, G. L.; Jahnatek, M.; Chepulskii, R. V.; Taylor, R. H.; Wang, S.; Xue, J.; Yang, K.; Levy, O.; Mehl, M. J.; Stokes, H. T.; Demchenko, D. O.; Morgan, D. AFLOW: An Automatic Framework for High-Throughput Materials Discovery. *Computational Materials Science***2012**, *58*, 218–226.

[35] Nelli, F. *Python data analytics with Pandas, NumPy, and Matplotlib*; Apress: Berkley, **2018**.

[36] Hunter, J. D. Matplotlib: A 2D Graphics Environment. *Computing in Science & Engineering* **2007**, *9*(3), 90–95.

[37] P4VASP. http://www.p4vasp.at/ (accessed **2019**).

APPENDICES

Appendix A. Model Structures of $Re_1Si_1Al_1$

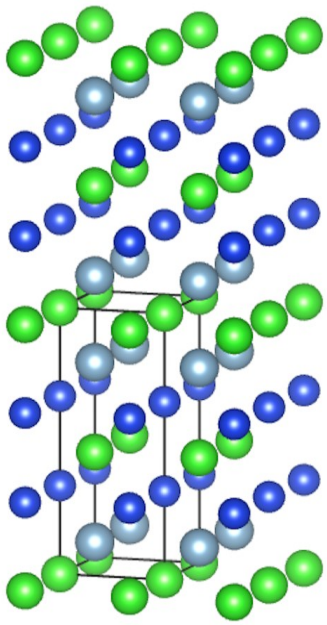

111_1

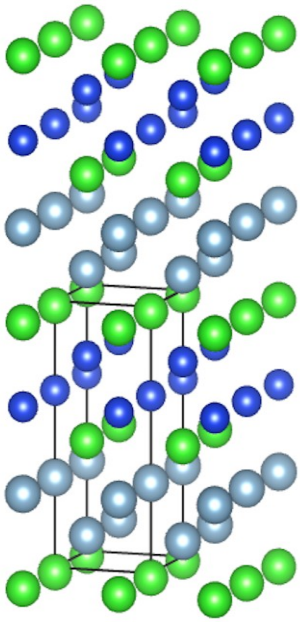

111_2

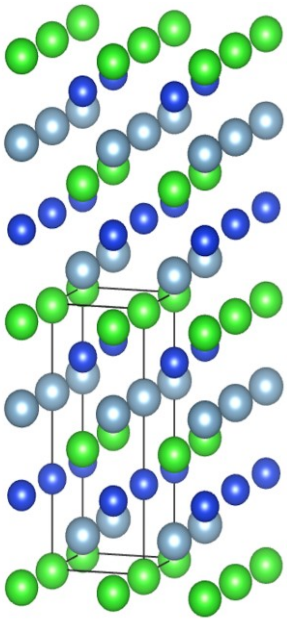

111_4

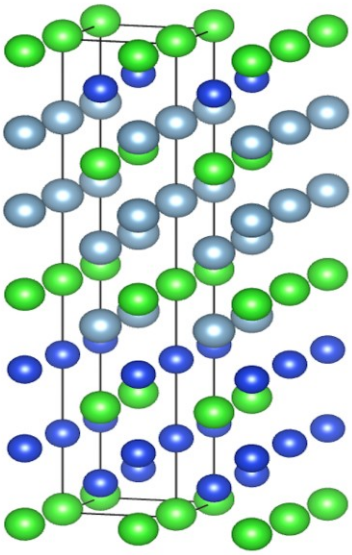

112_1

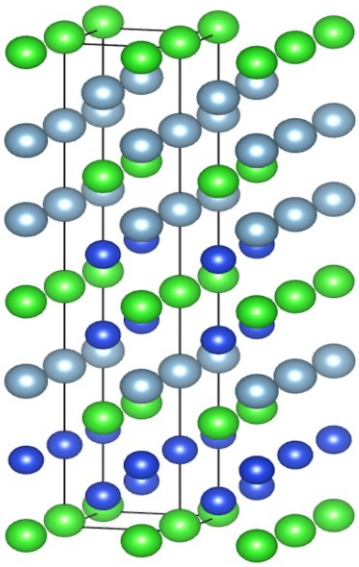

112_2

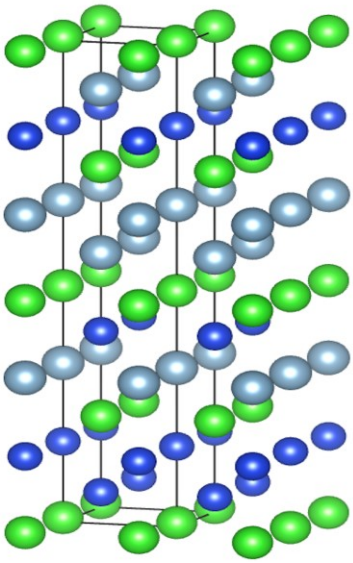

112_4

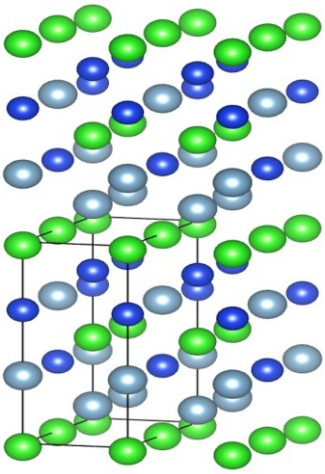

211_1

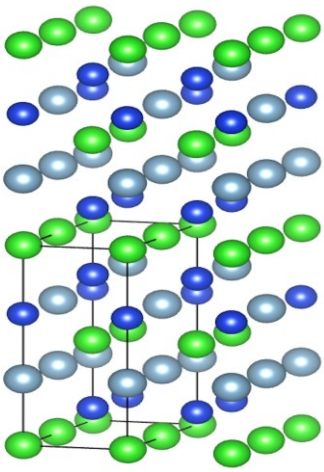

211_2

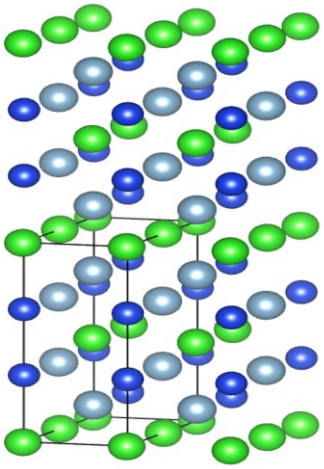

211_3

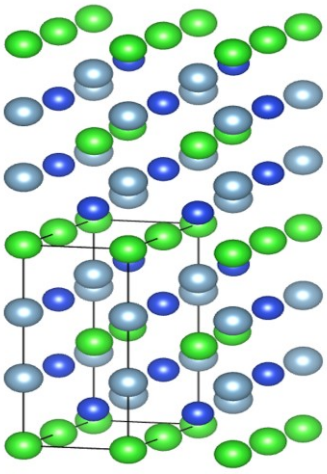

211_4

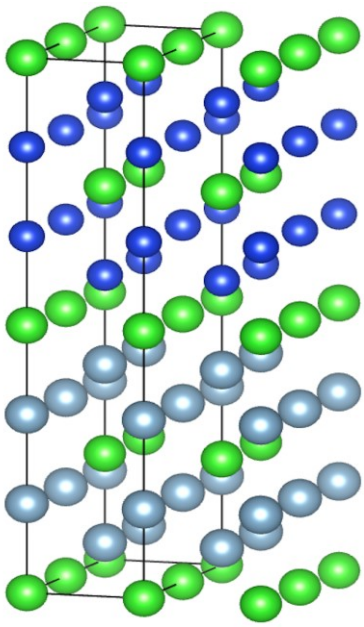

212_1

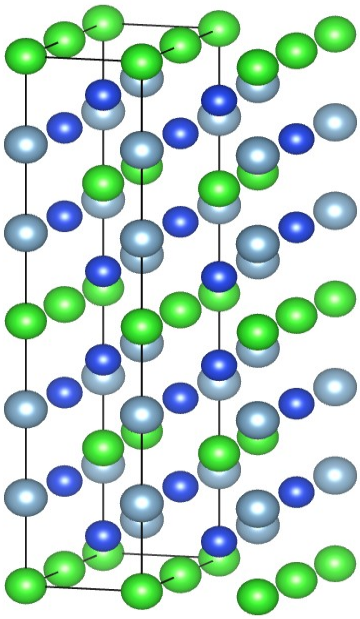

212_2

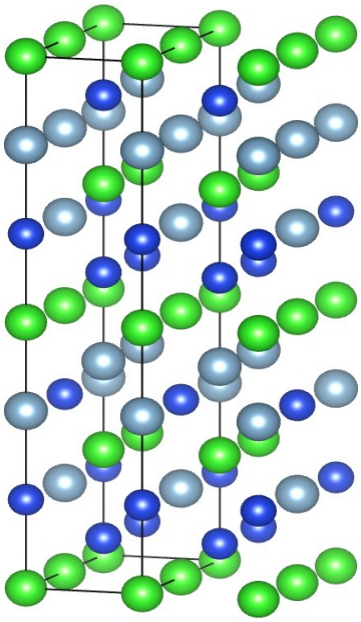

212_3

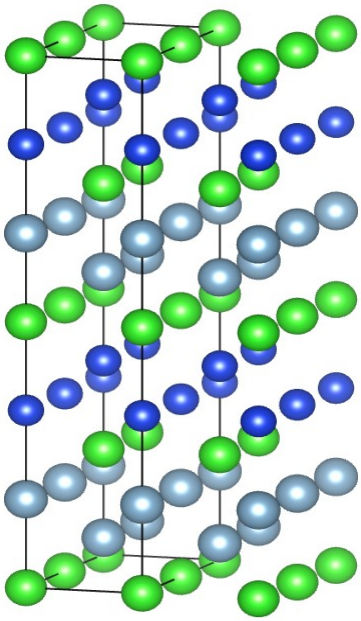

212_4

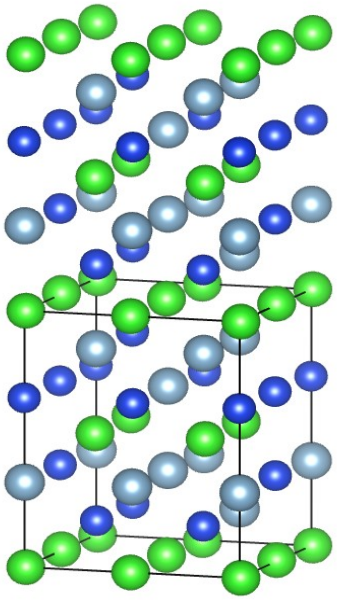

221_1

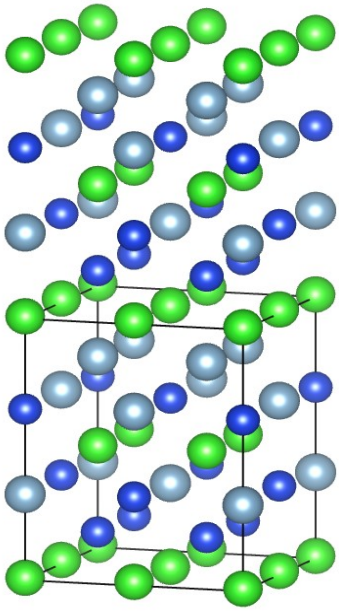

221_2

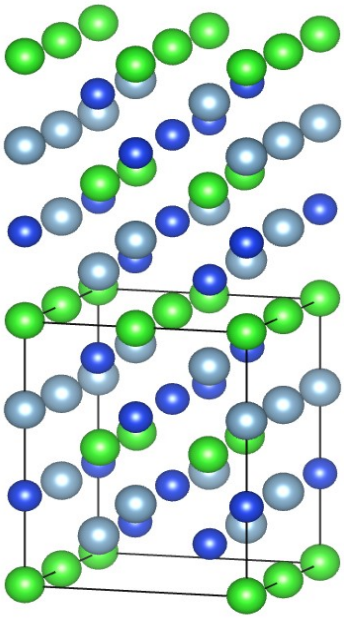

221_3

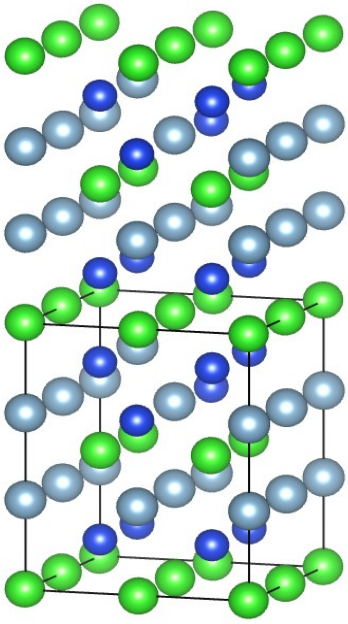

221_4

Appendix B. Model Structures of $Re_1Si_{0.75}Al_{1.25}$

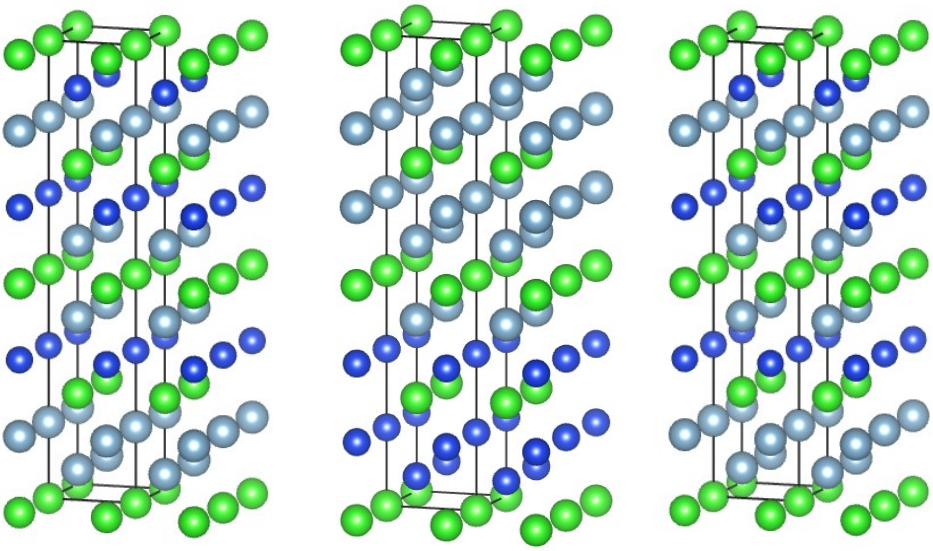

112_1 112_2 112_3

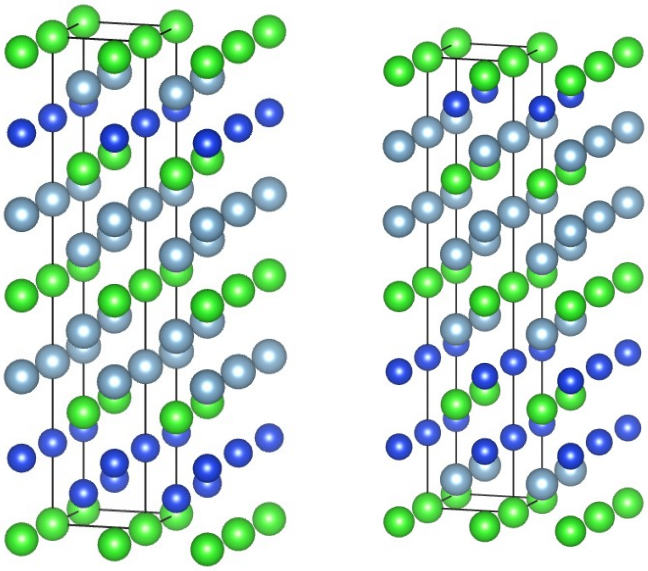

112_4 112_5

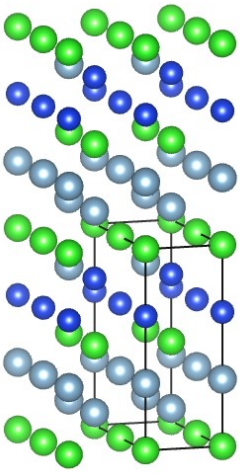

211_1

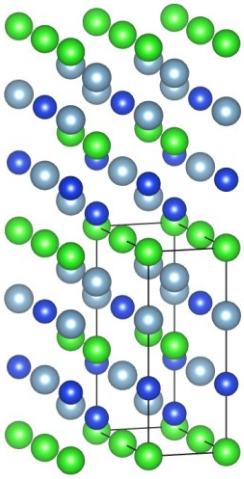

211_2

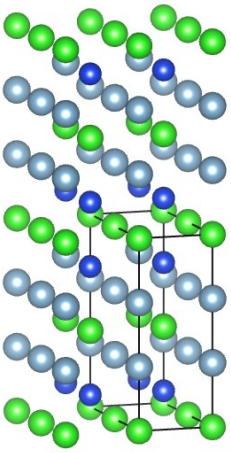

211_3

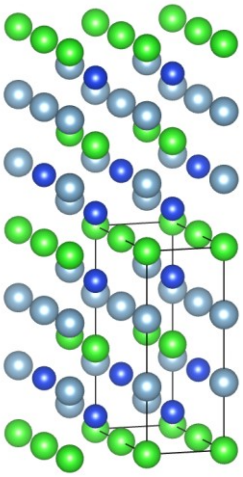

211_4

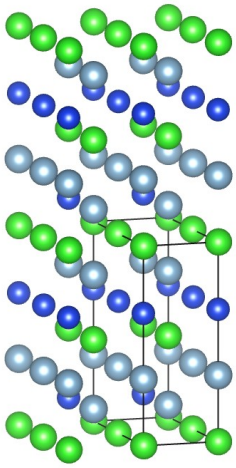

211_5

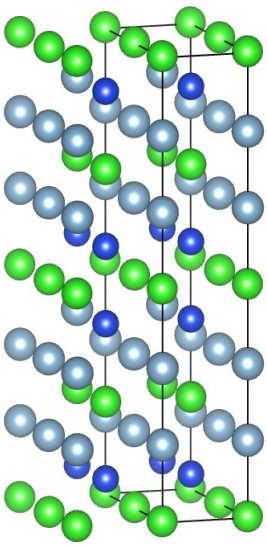

212_1

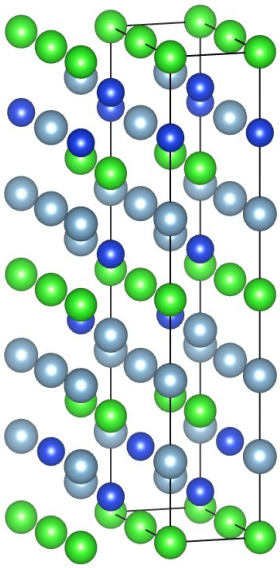

212_2

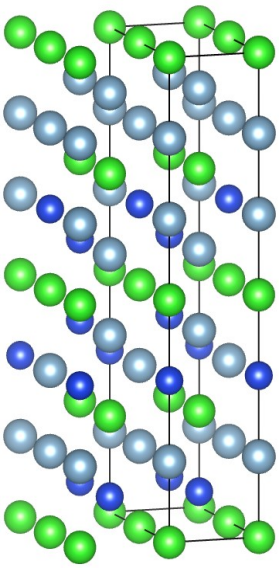

212_3

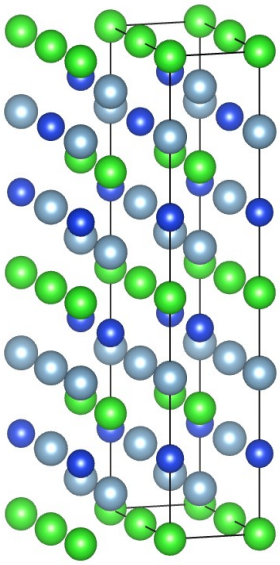

212_4

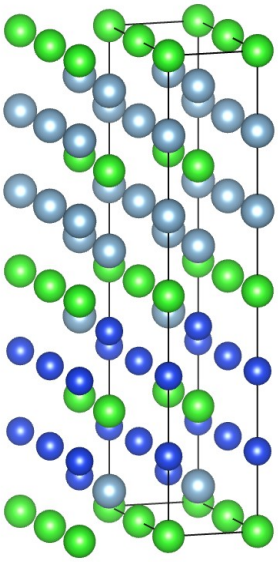

212_5

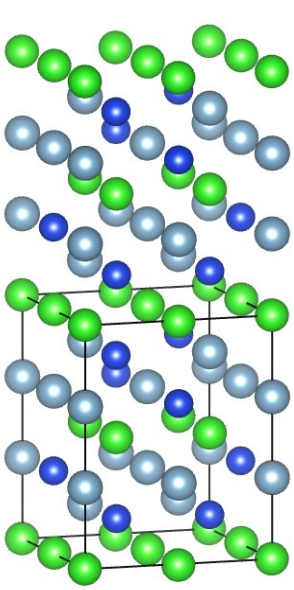

221_1

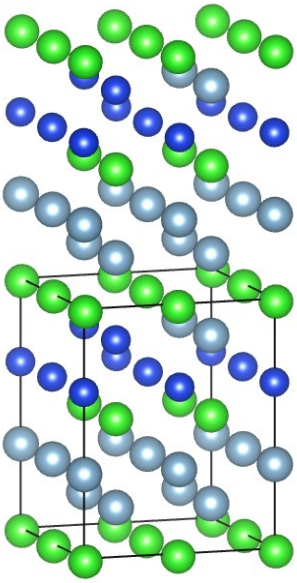

221_2

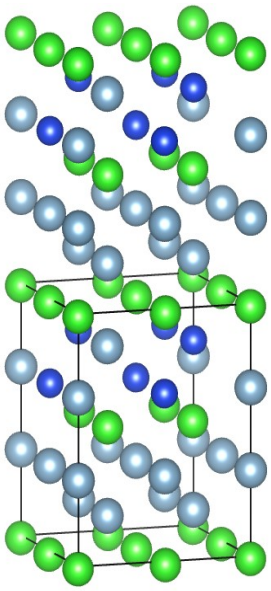

221_3

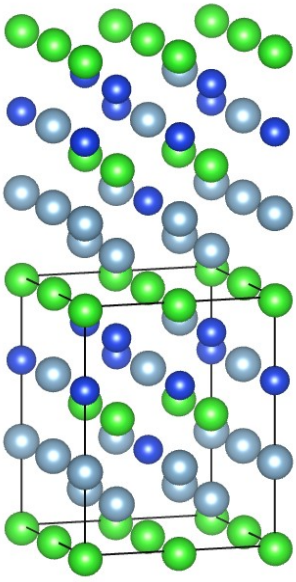

221_4

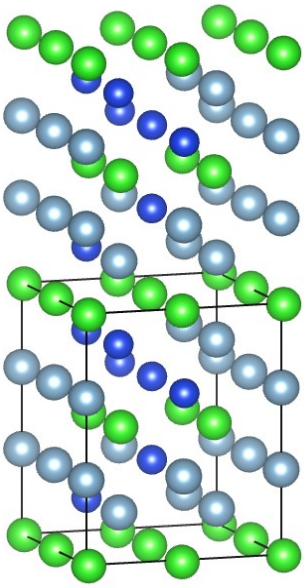

221_5

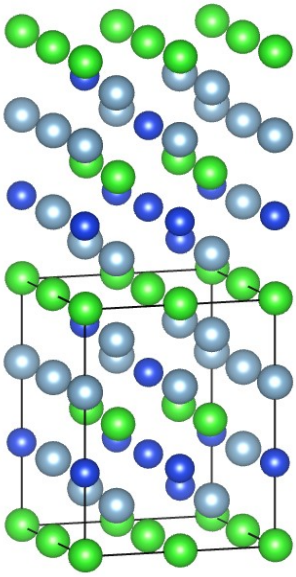

221_6

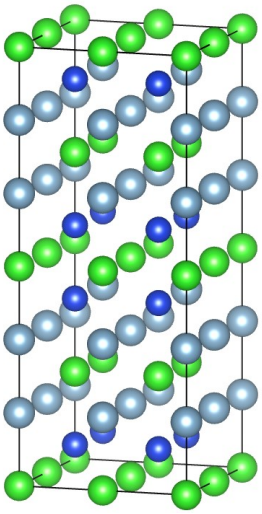

222_1

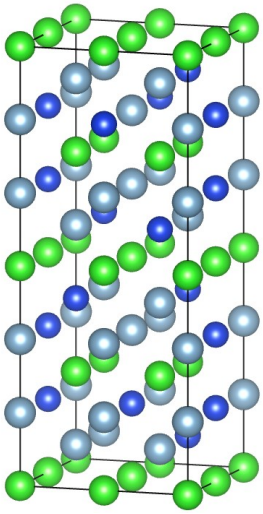

222_2

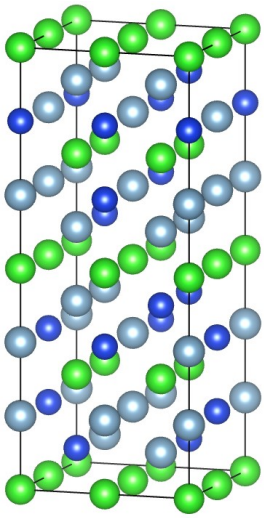

222_3

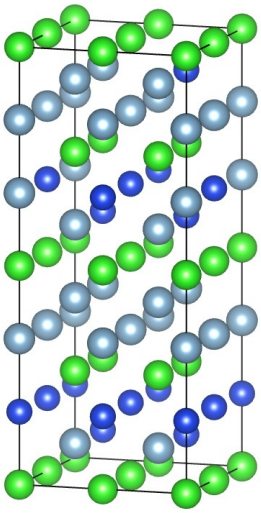

222_4

Appendix C. Python Code Example for Reading Band Structure Data

```
import matplotlib.pyplot as plt
import pandas as pd

name = input("\nWhat would you like the title of the graph to be?")

df = pd.read_csv("bands.csv")
df.columns = ["Kpoints","Energies"]

klst = []

start = 14    # starting point for the special kpoints
step = 16    # intervals between the special kpoints

for x in range(10):
    klst.append(df.at[start,"Kpoints"])
    start += step


x0 = [0,0]
x = [klst[0],klst[0]]
x1 = [klst[1],klst[1]]
x2 = [klst[2],klst[2]]
x3 = [klst[3],klst[3]]
x4 = [klst[4],klst[4]]
x5 = [klst[5],klst[5]]
x6 = [klst[6],klst[6]]
x7 = [klst[7],klst[7]]
x8 = [klst[8],klst[8]]
x9 = [klst[9],klst[9]]

print(klst)

x_y = [0, df["Kpoints"].max()] #length of the x_value in the bandstructure diagram

y = [-14,5]
y2 = [0,0]

ticks = ["Γ","X","M","Γ","Z","R","A","Z|X","R|M","A"] # needs to be changed accordingly
ticks2 = ['fermi level']


fig = plt.figure()

figure = df.plot(
```

```
        kind ='line',
        x="Kpoints",
        y="Energies",
        color = 'blue',
        legend = False
        )


plt.suptitle(name,fontsize = 17, fontweight = 'bold')  #activate this line whenever you want the plot to show something

ax = plt.subplot(111)


#ax.set_xlim(df["Kpoints"].max())
ax.set_xlim(0,1.16)
ax.set_ylim([-13,4])


plt.plot(x0,y,'g', linestyle = '--')
plt.plot(x,y,'g', linestyle = '--')
plt.plot(x1,y,'g',linestyle = '--')
plt.plot(x2,y,'g',linestyle = '--')
plt.plot(x3,y,'g',linestyle = '--')
plt.plot(x4,y,'g',linestyle = '--')
plt.plot(x5,y,'g',linestyle = '--')
plt.plot(x6,y,'g',linestyle = '--')
plt.plot(x7,y,'g',linestyle = '--')
plt.plot(x8,y,'g',linestyle = '--')
plt.plot(x_y,y2,'g',linestyle='--')


ax.set_xticks([x0[0],x[0],x1[0],x2[0],x3[0],x4[0],x5[0],x6[0],x7[0],x8[0]])
#ax.set_yticks([x9[0]])



ax.set_xticklabels((ticks[0],ticks[1],ticks[2],ticks[3],ticks[4],ticks[5],ticks[6],ticks[7],ticks[8],tic
ks[9]))

#ax.set_yticklabels((ticks2[0]))
ax.set_xlabel("Special Kpoints",fontsize = 15,fontweight = 'bold')
ax.set_ylabel("Energies (eV)",rotation = 90, fontsize = 15,fontweight = 'bold')

plt.show()
```

Appendix D. Selected Band Structures for $Re_1Si_1Al_1$

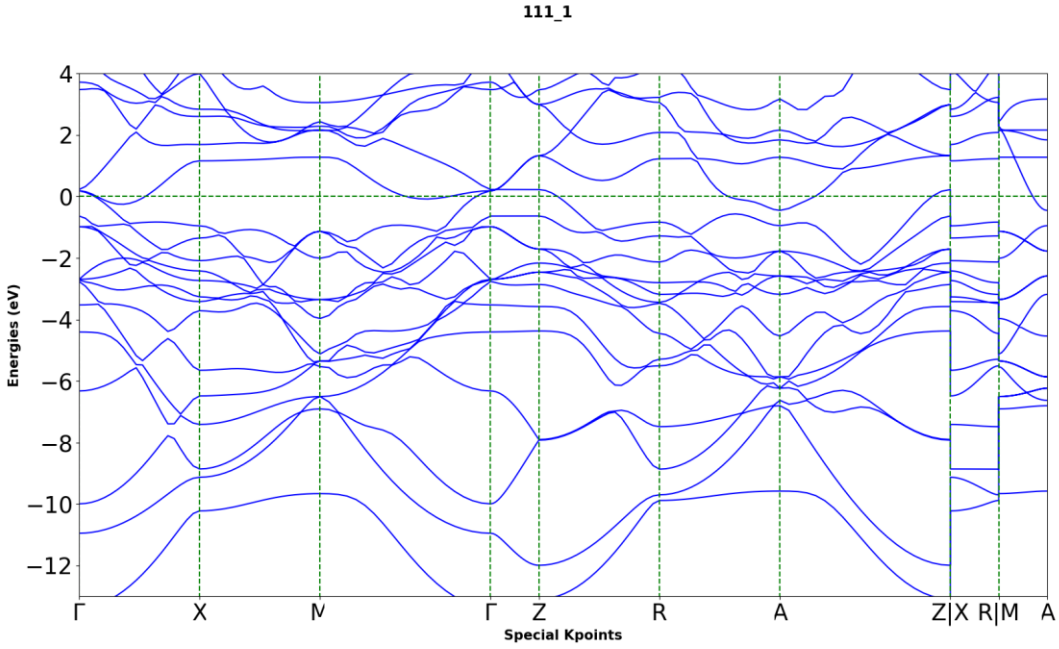

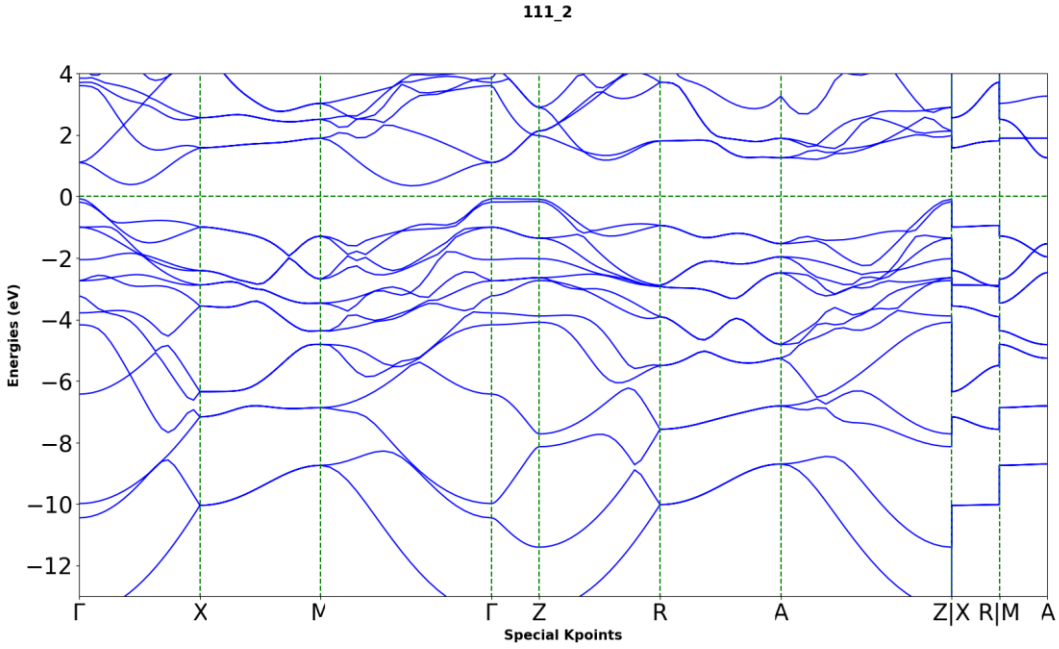

111_4

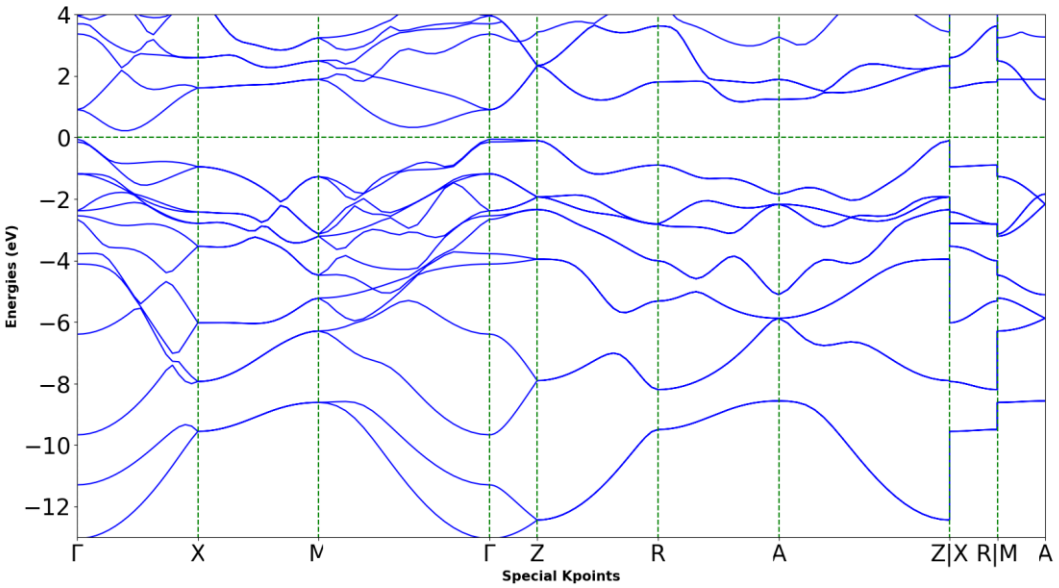
Energies (eV)
4
2
0
−2
−4
−6
−8
−10
−12
Γ
X
M
Γ
Z
R
A
Z|X
R|M
A
Special Kpoints

112_1

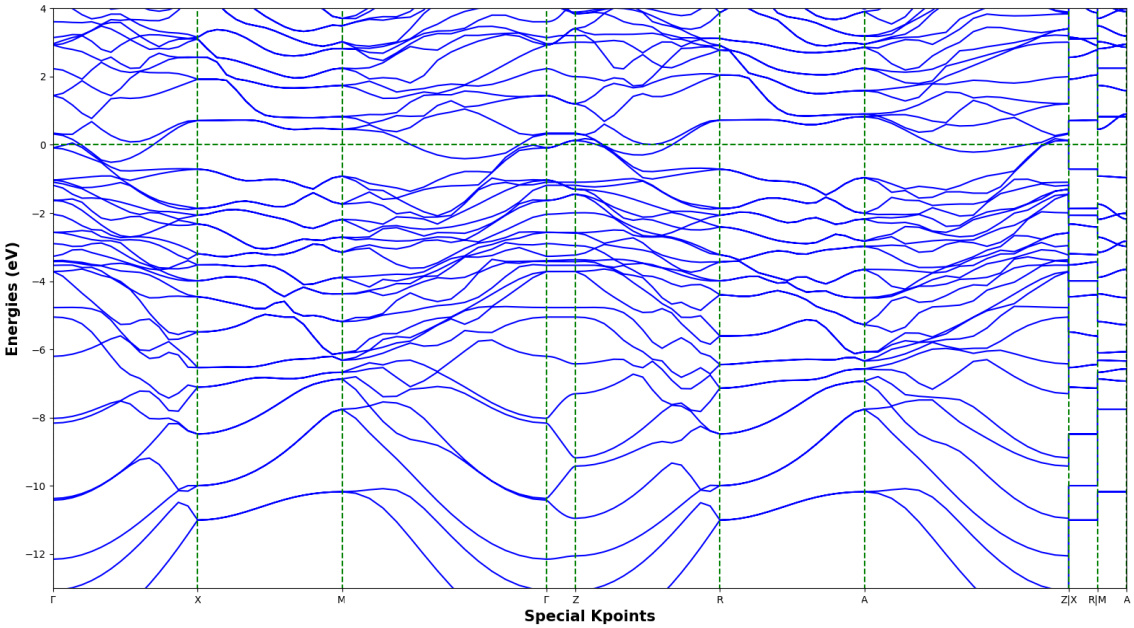
Energies (eV)
Γ
X
M
Γ
Z
R
A
Z|X
R|M
A
Special Kpoints

112_2

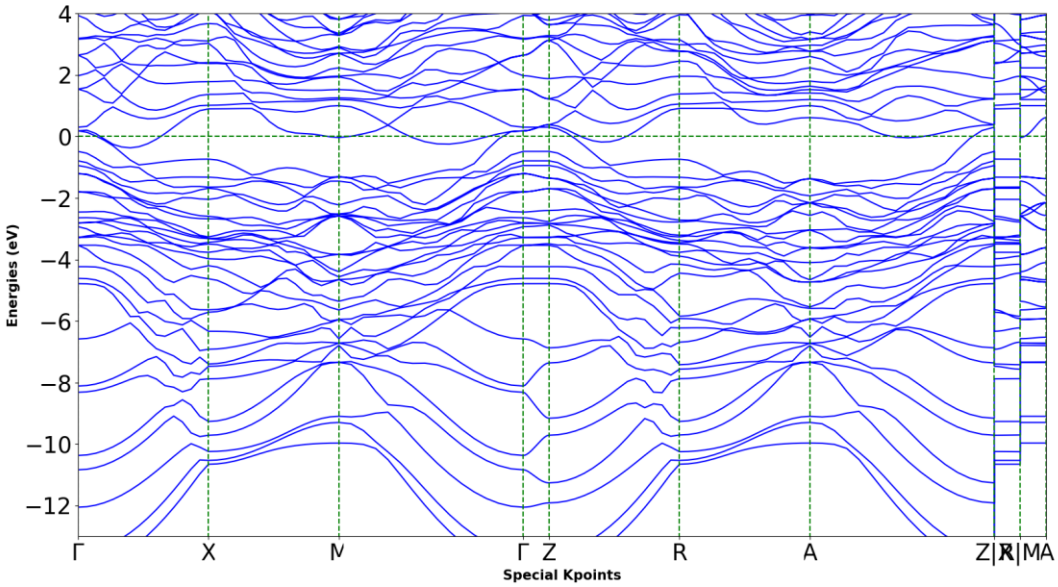
Energies (eV)
4
2
0
−2
−4
−6
−8
−10
−12
Γ
X
M
Γ
Z
R
A
Z|X
R|M
A
Special Kpoints

112_3

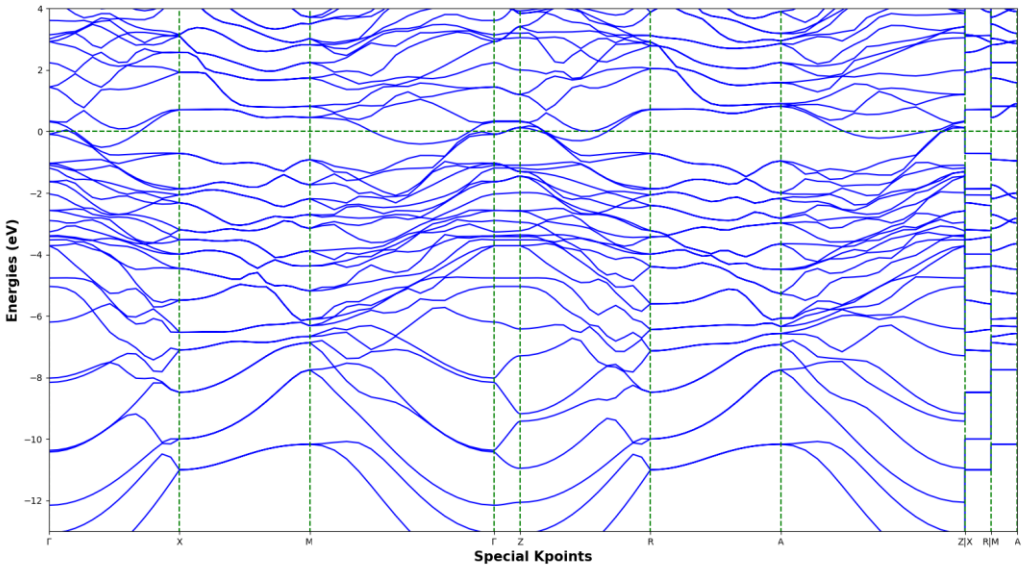
Energies (eV)
Special Kpoints

112_4

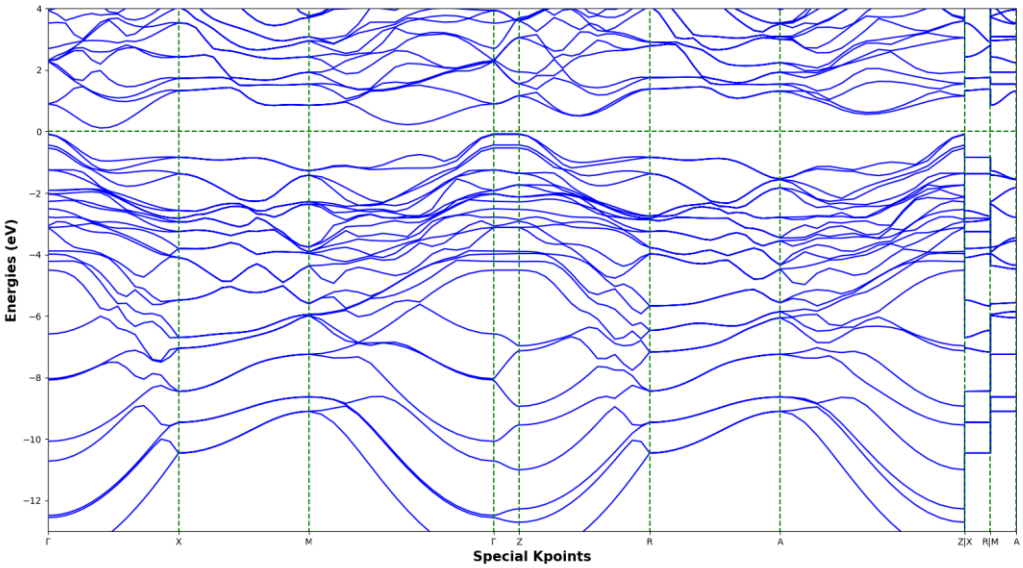
Energies (eV)
4
2
0
−2
−4
−6
−8
−10
−12
Γ
X
M
Γ
Z
R
A
Z|X
R|M
A
Special Kpoints

112_5

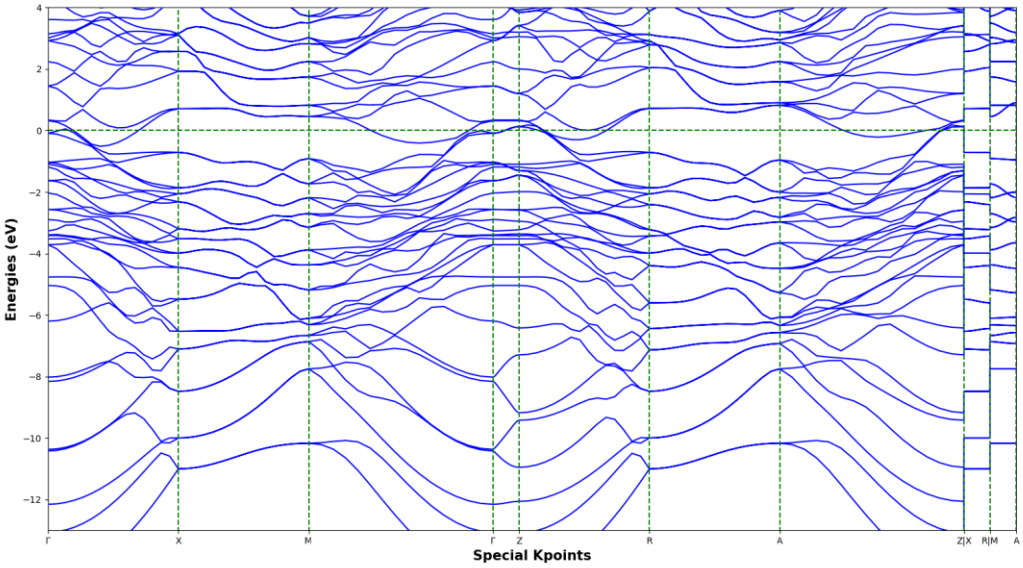
Energies (eV)
4
2
0
−2
−4
−6
−8
−10
−12
Γ
X
M
Γ
Z
R
A
Z|X
R|M
A
Special Kpoints

Appendix E. Selected Band Structures for $Re_1Si_{0.75}Al_{1.25}$

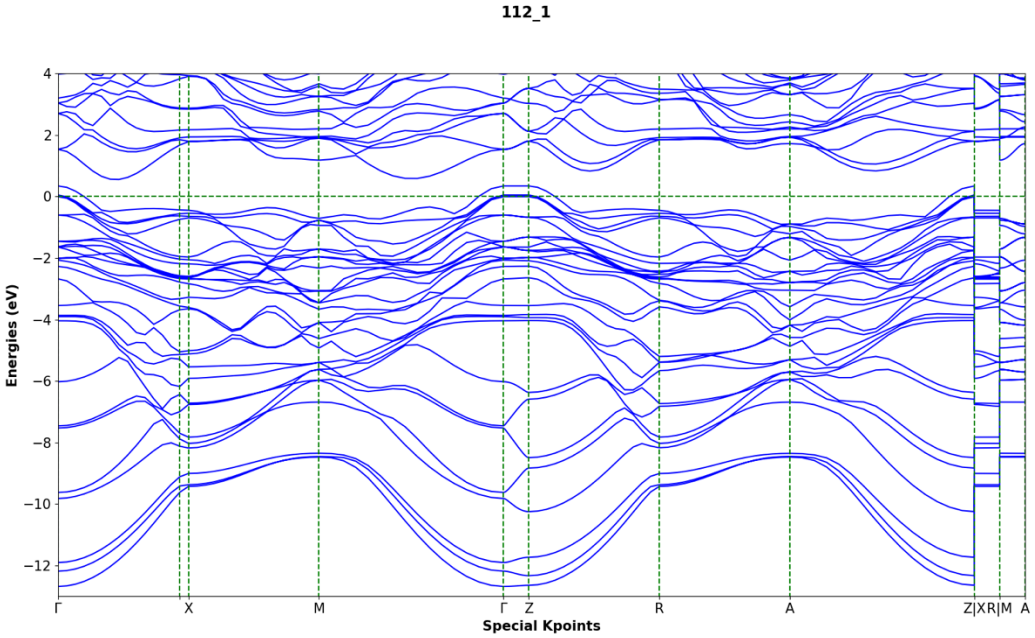

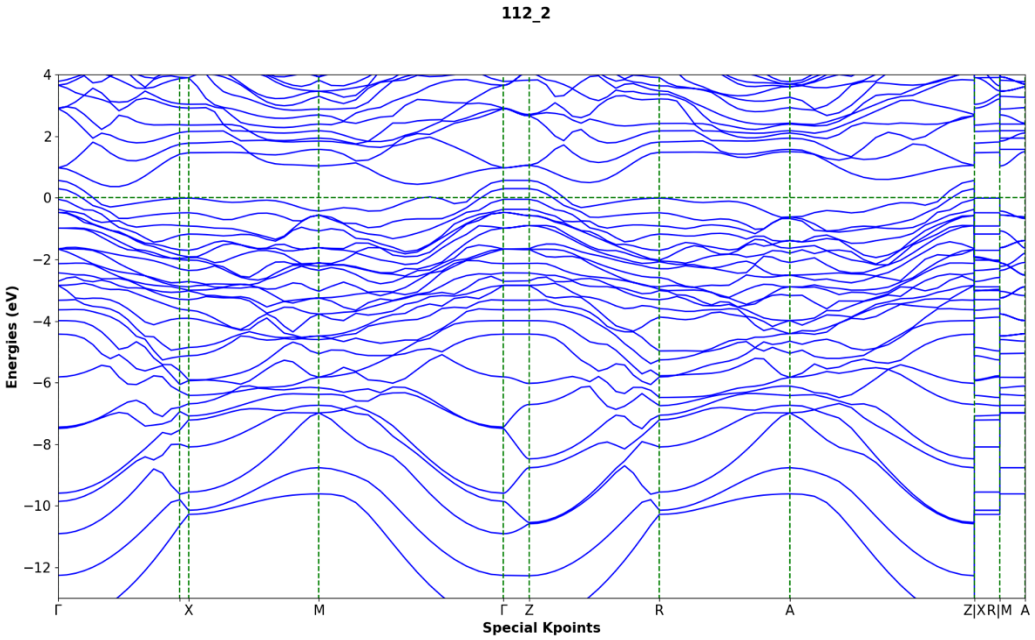

112_3

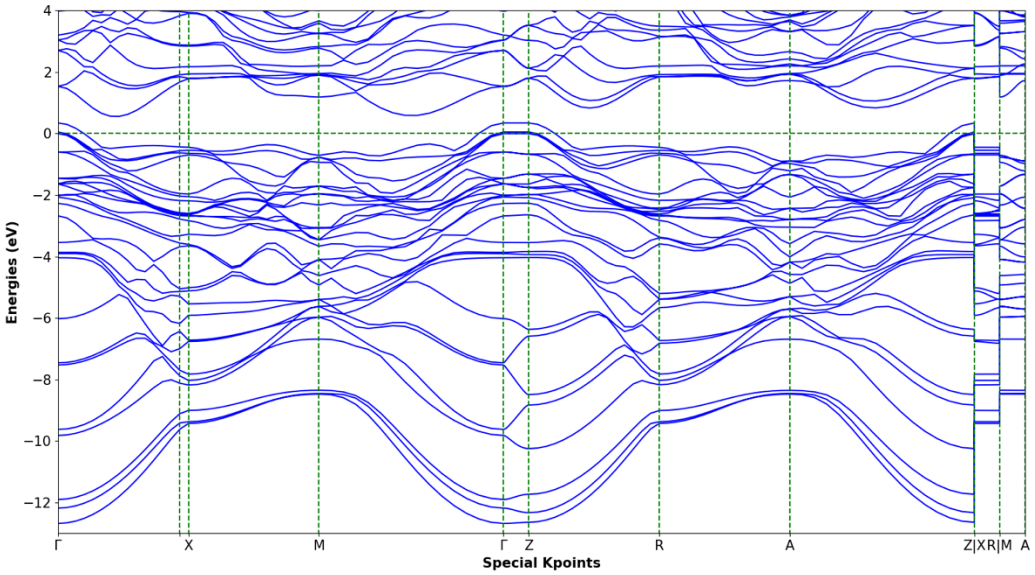
Energies (eV)
4
2
0
−2
−4
−6
−8
−10
−12
Γ
X
M
Γ
Z
R
A
Z|XR|M
A
Special Kpoints

112_4

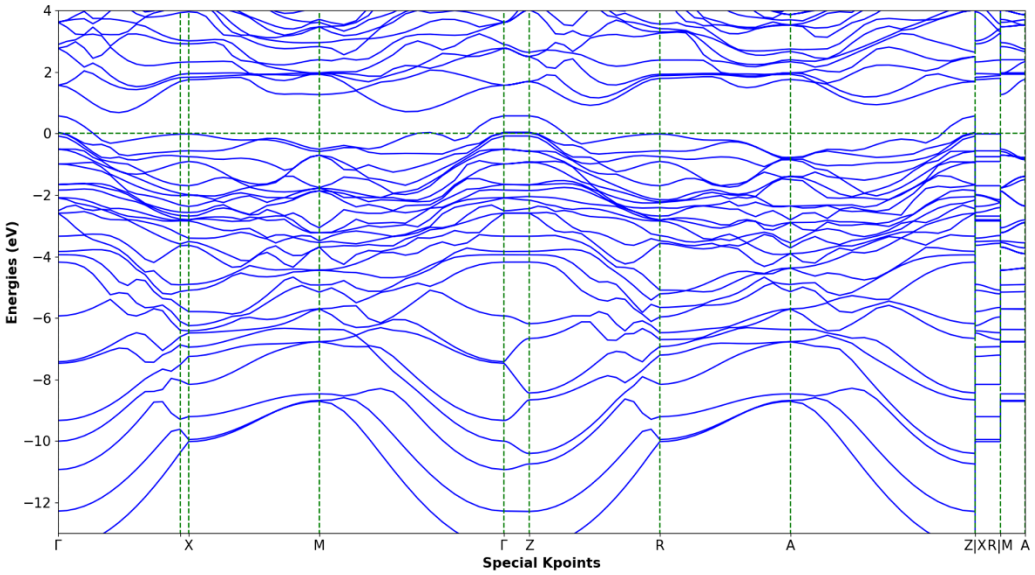
Energies (eV)
4
2
0
−2
−4
−6
−8
−10
−12
Γ
X
M
Γ
Z
R
A
Z|XR|M
A
Special Kpoints

112_5

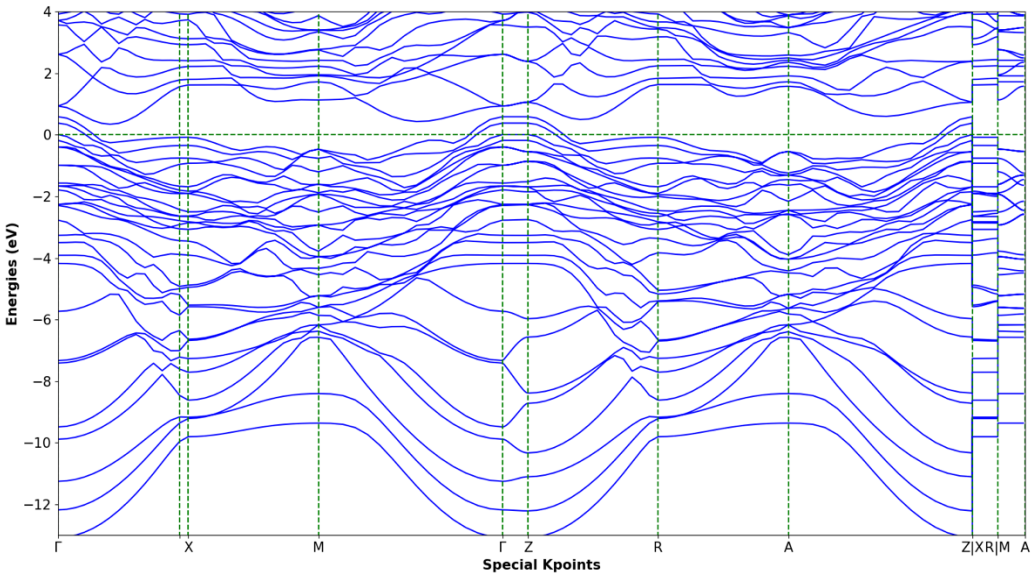
Energies (eV)
4
2
0
−2
−4
−6
−8
−10
−12
Γ
X
M
Γ
Z
R
A
Z|X
R|M
A
Special Kpoints

211_1

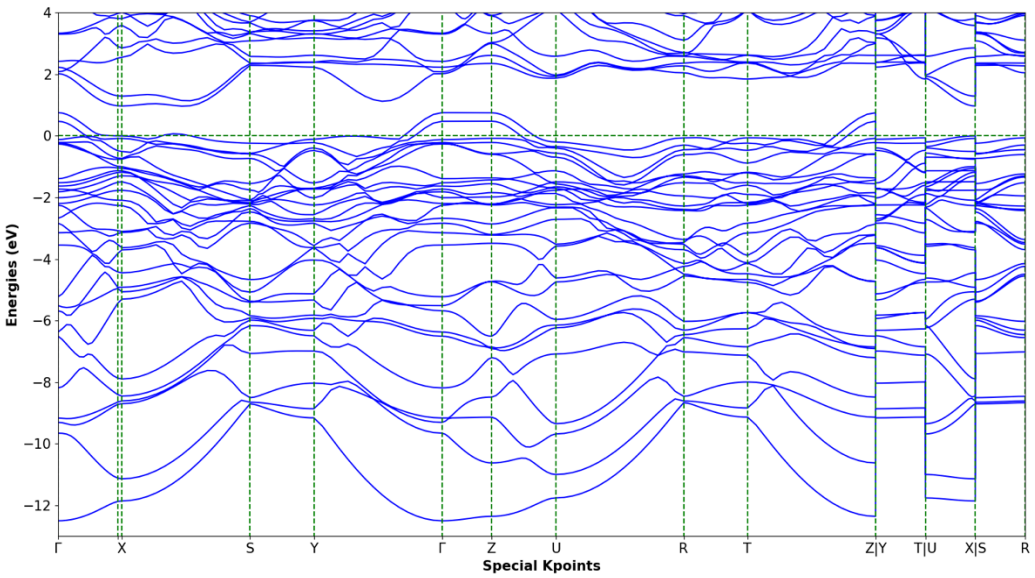
Energies (eV)
4
2
0
−2
−4
−6
−8
−10
−12
Γ
X
S
Y
Γ
Z
U
R
T
Z|Y
T|U
X|S
R
Special Kpoints

211_3

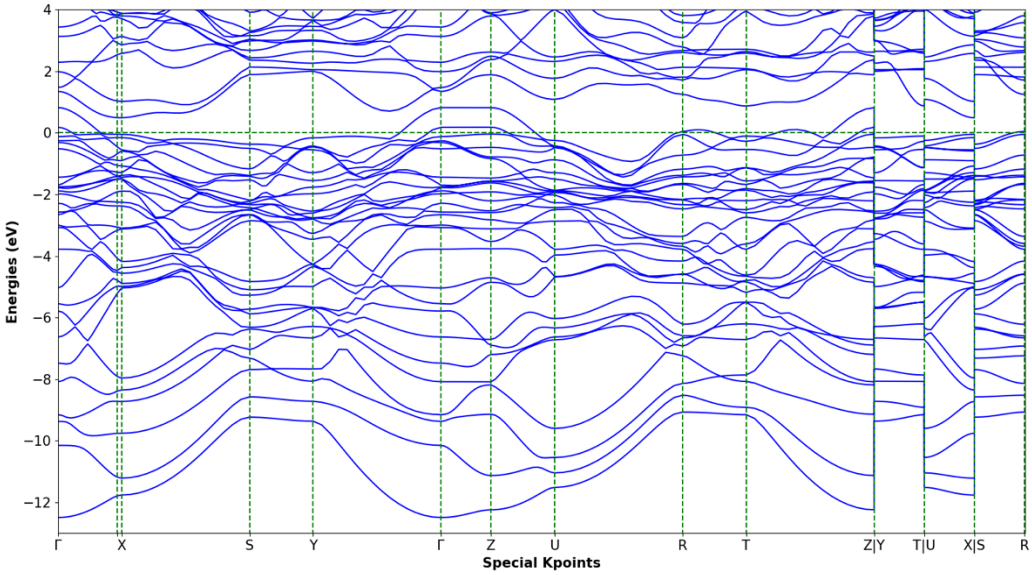
Energies (eV)
4
2
0
−2
−4
−6
−8
−10
−12
Γ
X
S
Y
Γ
Z
U
R
T
Z|Y
T|U
X|S
R
Special Kpoints

211_5

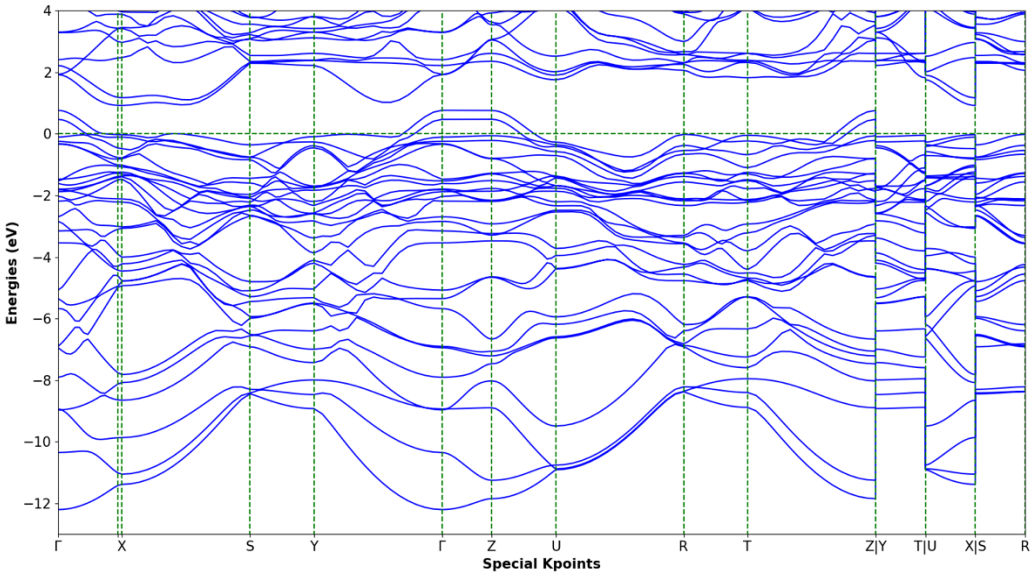
Energies (eV)
4
2
0
−2
−4
−6
−8
−10
−12
Γ
X
S
Y
Γ
Z
U
R
T
Z|Y
T|U
X|S
R
Special Kpoints